Evaluation of stratospheric NO2 retrieved from the Ozone Monitoring Instrument : intercomparison, diurnal cycle and trending

Evaluation of stratospheric NO_2 retrieved from the Ozone Monitoring Instrument: Intercomparison, diurnal cycle, and trending

Ruud J. Dirksen,[1,2] K. Folkert Boersma,[1,3] Henk J. Eskes,[1] Dmitry V. Ionov,[4,5] Eric J. Bucsela,[6] Pieternel F. Levelt,[1] and Hennie M. Kelder[3]

Received 24 August 2010; revised 6 February 2011; accepted 11 February 2011; published 22 April 2011.

[1] A 5+ year record of satellite measurements of nitrogen dioxide columns from the Ozone Monitoring Instrument (OMI) is evaluated to establish the quality of the OMI retrievals and to test our understanding of stratospheric NO_2. The use of assimilation techniques to retrieve stratospheric vertical columns of NO_2 from OMI slant column observations is described in detail. Over remote areas the forecast model state is generally within 0.15×10^{15} molecules/cm^2 of the analysis. Dutch OMI NO_2 (DOMINO) and Standard Product (SP) stratospheric NO_2 columns agree within 0.3×10^{15} molecules/cm^2 (13%) with independent, ground-based measurements. This is comparable to the level of consistency (15–20%) among ground-based techniques. On average, DOMINO stratospheric NO_2 is higher than SP by 0.2×10^{15} molecules/cm^2, but larger differences occur on the synoptic scale. Overlapping OMI orbits poleward of 30° enabled us to extract information on the diurnal variation in stratospheric NO_2. We find that in the Arctic, the daytime increase of NO_2 has a distinct seasonal dependence that peaks in spring and fall. Daytime increase rates inside the denoxified Arctic polar vortex are low, but we find high rates ($>0.4 \times 10^{15}$ molecules/cm^2/h) outside the vortex. A multilinear regression to the DOMINO record shows a distinct quasi-biennial oscillation (QBO) signal in stratospheric NO_2 columns over the tropics. The QBO's amplitude is comparable to the annual cycle and stronger over the Southern Hemisphere than over the Northern Hemisphere. We infer near-identical trends from DOMINO observations (+0.4%/decade) as from ground-based instrumentation over Lauder (+0.6%/decade) in the 2004–2010 period.

Citation: Dirksen, R. J., K. F. Boersma, H. J. Eskes, D. V. Ionov, E. J. Bucsela, P. F. Levelt, and H. M. Kelder (2011), Evaluation of stratospheric NO_2 retrieved from the Ozone Monitoring Instrument: Intercomparison, diurnal cycle, and trending, *J. Geophys. Res.*, *116*, D08305, doi:10.1029/2010JD014943.

1. Introduction

[2] Nitrogen dioxide (NO_2) is an important trace gas in the atmosphere because of its role in the photochemistry of ozone in the stratosphere and in the troposphere. NO + NO_2 (NO_x) in the stratosphere originates from the oxidation of N_2O in the middle stratosphere. NO + NO_2 destroy ozone catalytically, but they can also suppress ozone depletion by converting reactive chlorine and hydrogen compounds into unreactive reservoirs such as $ClONO_2$ and HNO_3. Monitoring of stratospheric NO_2 thus provides important support to monitoring of the ozone layer. Furthermore, outstanding questions exist about long-term changes in stratospheric NO_2 reported for instance from New Zealand [*Liley et al.*, 2000] and northern Russia [*Gruzdev*, 2008]. In the troposphere, NO_x is mainly produced by combustion, emission by soils, and lightning. Tropospheric NO_x oxidizes rapidly, leading to the formation of ozone and aerosols. These secondary pollutants have highly uncertain effects on climate [*Intergovernmental Panel on Climate Change*, 2007], influence the oxidizing capacity of the troposphere, and affect human health. Global mapping of tropospheric NO_2 concentrations provides important constraints on the temporal behavior of NO_x emissions.

[3] Satellite remote sensing is used for measuring stratospheric as well as tropospheric NO_2 amounts. Stratospheric NO_2 has been measured by a number of satellites since the 1980s, e.g., SME (Solar Mesosphere Explorer) [*Mount et al.*, 1984], which first used the DOAS approach, SAGE-II/III

[1]Royal Netherlands Meteorological Institute, De Bilt, Netherlands.
[2]Now at Institut für Weltraumwissenschaften, Freie Universität Berlin, Berlin, Germany.
[3]Department of Applied Physics, Eindhoven University of Technology, Eindhoven, Netherlands.
[4]Department of Atmospheric Physics, Research Institute of Physics, St. Petersburg, Russia.
[5]LATMOS, CNRS, University of Versailles Saint Quentin, Guyancourt, France.
[6]SRI International, Menlo Park, California, USA.

0148-0227/11/2010JD014943

(Stratospheric Gas and Aerosol Experiment) [*Chu and McCormick*, 1986], HALOE (Halogen Occultation Experiment) [*Gordley et al.*, 1996], and POAM (Polar Ozone and Aerosol Measurement) [*Randall et al.*, 1998]. More recently, retrievals from the nadir-viewing UV-Vis spectrometers GOME (Global Ozone Monitoring Experiment) [*Burrows et al.*, 1999] and its successor GOME-2 [*Munro et al.*, 2006], SCIAMACHY (SCanning Imaging Absorption SpectroMeter for Atmospheric CHartographY) [*Bovensmann et al.*, 1999], and OMI (Ozone Monitoring Instrument) [*Levelt et al.*, 2006a] have provided information on both stratospheric and tropospheric NO_2. Over unpolluted regions typically more than 90% of the observed NO_2 resides in the stratosphere, but over industrialized continental regions this fraction can range from 10 to 50%, depending on the degree of pollution. A challenge for the retrieval algorithms is the separation of the stratospheric and tropospheric contribution to the total NO_2 absorption inferred from the spectral measurements. Inaccuracies in this separation not only affect the stratospheric measurements themselves, but also the tropospheric retrievals that rely on residual techniques. Current methods to estimate stratospheric NO_2 use chemistry-transport models [*Boersma et al.*, 2004; *Richter et al.*, 2005], filtering techniques based on subsets of satellite measurements [*Bucsela et al.*, 2006], or independent measurements of stratospheric NO_2 [*Beirle et al.*, 2010]. These techniques need to be thoroughly tested against independent observations, which is one of the goals of this study.

[4] In this work we focus on OMI stratospheric NO_2. The OMI retrievals start with total NO_2 slant column densities (SCDs), inferred from the instrument's spectrally resolved measurements in the visible. The total slant columns represent the integrated concentration of NO_2 along the effective light path through the atmosphere. Since photons in the visible traverse the lower atmosphere, there can be a significant contribution from tropospheric NO_2 to the total slant column. In the Dutch OMI NO_2 retrieval (DOMINO) *Boersma et al.* [2007], the stratospheric component of the NO_2 slant column is estimated by data assimilation of OMI slant columns in the TM4 chemistry-transport model. In the NASA/KNMI retrieval (Standard Product, *Bucsela et al.* [2006]), the stratospheric component is estimated by fitting a second-order Fourier function in the zonal direction to a 24 h composite of OMI observations. Both methods use air mass factors (AMFs) to convert stratospheric slant columns into vertical columns, but the AMFs are calculated with different radiative transfer models, and use different a priori information on the vertical distribution of stratospheric NO_2.

[5] In order to test and improve the stratospheric NO_2 information derived from OMI, the present work evaluates the two different OMI retrievals. We compare OMI stratospheric NO_2 from both retrievals with independent measurements taken at 14 remote NDACC (Network for the Detection of Atmospheric Composition Change) stations around the world. Doing so, we used UV-Vis measurements from the SAOZ (Système d'Analyse par Observations Zénithal) network, a collection of near-identical collectively operated instruments that is part of NDACC, UV-Vis measurements from other NDACC stations as well as FTIR observations.

[6] We subsequently evaluate the ability of the retrieval algorithms to observe spatial and temporal variability in stratospheric NO_2. We will show that the Dutch OMI NO_2 retrieval captures spatial and temporal variations in stratospheric NO_2 induced by planetary waves, and also the daytime buildup of stratospheric NO_2 resulting from the photolysis of N_2O_5. Furthermore, we will analyze the 5 year record of OMI stratospheric NO_2 columns and discuss signatures of the quasi-biennial oscillation apparent over tropical and midlatitudes.

2. OMI Stratospheric NO_2 Data

2.1. OMI

[7] The Dutch-Finnish Ozone Monitoring Instrument (OMI) is a UV-Vis imaging spectrometer that records the backscattered radiance from the Earth's atmosphere in three spectral channels between 264 and 504 nm at an average spectral resolution of 0.5 nm. It combines a wide longitudinal swath (2600 km) with high spatial resolution (24 × 13 km^2 at nadir). OMI is part of the NASA EOS-Aura mission (launched July 2004) which is in a Sun-synchronous ascending node orbit that crosses the equator at 1340 local time (LT). In sections 2.2 and 2.3 we describe the algorithms of the DOMINO and the Standard Product. The DOMINO product is available at http://www.temis.nl/airpollution/no2.html, the Standard Product is available at http://daac.gsfc.nasa.gov/Aura/data-holdings/OMI/index.shtml. Both products use OMI NO_2 slant columns as input, and these are also included in the final product. A detailed description of OMI's scientific objectives is given by *Levelt et al.* [2006b], instrument details are available from *Dobber et al.* [2006].

2.2. Dutch OMI NO_2 (DOMINO) Retrieval

[8] The retrieval of the stratospheric and tropospheric NO_2 vertical columns by the DOMINO algorithm is the result of a multistep process. In the first step, slant columns of NO_2 are retrieved with the DOAS (Differential Optical Absorption Spectroscopy) [*Platt and Stutz*, 2008] method, by minimizing the differences between modeled and observed Earth reflectance spectra. The minimization is performed in the 405–465 nm spectral window, taking into account absorption by NO_2, ozone, and water vapor, the Ring effect and a third-order polynomial that describes the background of the reflectance spectrum. The NO_2 cross section spectrum for 220 K is taken from *Vandaele et al.* [1998]. The retrieval method accounts for the temperature sensitivity of the NO_2 spectrum by applying a correction for the difference between the effective temperature of NO_2 along the light path derived from ECMWF meteorological analyses and modeled profiles, and the 220 K of the NO_2 absorption cross-section spectrum [*Boersma et al.*, 2004]. Earth reflectance spectra follow from dividing the Earth radiance measurements by the OMI-measured solar irradiance. For signal-to-noise considerations a fixed solar irradiance spectrum has been constructed from daily irradiance measurements taken in 2005. Calibration errors resulting from, amongst others, the limited signal-to-noise of the solar irradiance measurements cause systematic enhancements of NO_2 slant columns at specific viewing angles, that show up as stripes along the orbit [*Boersma et al.*, 2007]. An

improved calibration approach, with a better correction of the CCD detector's dark current, significantly reduced these stripes [*Dobber et al.*, 2008]. The data used in this study have been processed with this improved dark current calibration. The precision of the retrieved NO_2 slant columns has been estimated to be 0.7×10^{15} molecules/cm^2 [*Boersma et al.*, 2007], which corresponds to approximately 10% of the unpolluted, and <5% of the polluted, slant column.

[9] In the second step, OMI NO_2 slant columns are assimilated in the TM4 chemistry transport model [*Dentener et al.*, 2003]. The assimilation procedure is described in section 2.2.1. In the third and final step the assimilated stratospheric slant column is subtracted from the total slant column and the remaining tropospheric slant column is converted into a vertical column by dividing by the tropospheric air mass factor (AMF). The AMF is defined as the ratio of slant column density of the absorber along the (slant) optical path to the vertical column density. The AMF is calculated using the DAK [*de Haan et al.*, 1987; *Stammes*, 2001] radiative transfer model that takes into account viewing geometry, the absorber's vertical profile shape, terrain height, surface albedo, clouds, and Rayleigh scattering (including multiple scattering effects). The AMF depends on the tropospheric NO_2 profile, which is taken from space-time collocated TM4 model results. The spectral fitting and the tropospheric AMF have been studied in detail elsewhere [*Boersma et al.*, 2002, 2004, 2007] and we will now focus on the assimilation procedure to estimate stratospheric NO_2.

2.2.1. Estimation of the Stratospheric NO_2 Column

2.2.1.1. TM4

[10] We use the TM4 chemistry transport model (CTM) for the assimilation of OMI NO_2 slant columns. The assimilation system operates at a resolution of 3° × 2° (longitude × latitude), with 35 sigma pressure levels up to 0.38 hPa in the vertical direction. After 1 February 2006 the model configuration was changed to 34 pressure levels, driven by a change in the sigma levels of the meteorological input. TM4 uses forecasted and analyzed 6-hourly meteorological fields, (3-hourly for boundary layer fields) from the European Centre for Medium Range Weather Forecast (ECMWF) operational model. These fields include global distributions of wind, temperature, surface pressure, humidity, cloud cover and (liquid and ice) water content, and precipitation. Mass conserving preprocessing of the meteorological input is performed as described by *Bregman et al.* [2003]. The physical processes included in determining tracer evolution are mass conserved advection, convective transport, boundary layer diffusion, photolysis and dry and wet deposition. NO_x emissions are based on the EU POET (Precursors of Ozone and their Effects on the Troposphere) database for 1997 [*Olivier et al.*, 2003], yielding a global total of 46 Tg N/yr. Chemical processes in the troposphere are governed by the Carbon Bond Mechanism 4 (CBM-4) chemistry scheme that includes nonmethane hydrocarbons to account for loss by reaction with OH [*Houweling et al.*, 1998].

[11] The CBM-4 scheme accounts for O_x-NO_x-HO_x chemical reactions in the stratosphere, including the conversion of NO and NO_2 to N_2O_5 and HNO_3. Other chemical aspects, such as the photolysis of N_2O and reactions with halogens such as bromine and chlorine are missing. Some effects of the simplified chemistry in the stratosphere are compensated for by constraining the modeled concentrations to observed climatological values in the middle/upper stratosphere. Above 50 hPa in the tropics and above 100 hPa in the extratropics, ozone concentrations are nudged to mean observed values taken from the Fortuin-Kelder climatology [*Fortuin and Kelder*, 1998] (scaled with the TOMS total O_3 column for 1997) with a relaxation time of 2–5 days, depending on latitude. At 10 hPa, stratospheric HNO_3 is nudged to the UARS-derived O_3/HNO_3 ratios for 1992 (B. Bregman, personal communication, 1997), with a characteristic relaxation time of 2 months. This is a modification of the original TM4 code, where the UARS O_3/HNO_3 ratio is simply prescribed. The long relaxation time prevents the nudging from strongly interfering with the NO_x analysis resulting from the data assimilation discussed below. Above 10 hPa, the NO_x volume mixing ratio is nudged to its modeled value at 10 hPa, again with characteristic relaxation time of 2 months. The prescribed 10 hPa HNO_3 mixing ratio constitutes the effective source of stratospheric NO_x in TM4.

2.2.1.2. Data Assimilation

[12] The purpose of the assimilation is to regularly update the TM4 simulation of the three-dimensional NO_2 distribution with available measurement data in such a way that the model simulation of the stratospheric NO_2 column is in close agreement with the OMI measurements. The assimilation also provides a realistic error estimate for the stratospheric NO_2 column (see below). The assimilation scheme is based on the Kalman filter technique, with a prescribed parameterization of the horizontal correlations between forecast errors to reduce computational effort. A schematic layout of the assimilation procedure is presented in Figure 1. The upper loop in Figure 1 illustrates the TM4 simulation of the three-dimensional NO_2 field with a time step Δt (30 min in TM4). If NO_2 slant columns are available with a measurement time within 15 min of the model time, the model field is updated by the Kalman filter. In the Kalman filter update, the forecast model state is adjusted toward the observations, replacing the forecast with the analysis. This analyzed profile field $\vec{x}_a$ includes NO_2 in both troposphere and stratosphere, and is calculated from the forecast $\vec{x}_f$ and the 2-D field of superobservations $\vec{y}$ (explained below) by

$$\vec{x}_a = \vec{x}_f + \mathbf{P}\mathbf{H}^T\left(\mathbf{H}\mathbf{P}\mathbf{H}^T + \mathbf{R}\right)^{-1}(\vec{y} - \vec{y}_m), \quad (1)$$

with matrix **H** the observation operator, **P** the forecast error covariance matrix, and **R** the combined observation and representativeness error covariance [*Eskes et al.*, 2003]. The role of **H**, **P** and **R** will be discussed in more detail below. The term $\mathbf{P}\mathbf{H}^T(\mathbf{H}\mathbf{P}\mathbf{H}^T + \mathbf{R})^{-1}$ determines the most likely adjustment of the model state, given the difference between observed and forecast model column ($\vec{y} - \vec{y}_m$, observation minus forecast, O − F). Note that the total slant column $\vec{y}$ includes the NO_2 present in both troposphere and stratosphere. The relative size of the adjustment depends on the ratio between the uncertainties in the model forecast and observations, and the model analysis will closely follow the observations when this ratio is large.

[13] The observation operator **H** is proportional to the averaging kernel [*Eskes and Boersma*, 2003], a 35-element vector that contains the sensitivity of OMI to NO_2 in each model layer. The scalar product of the observation operator

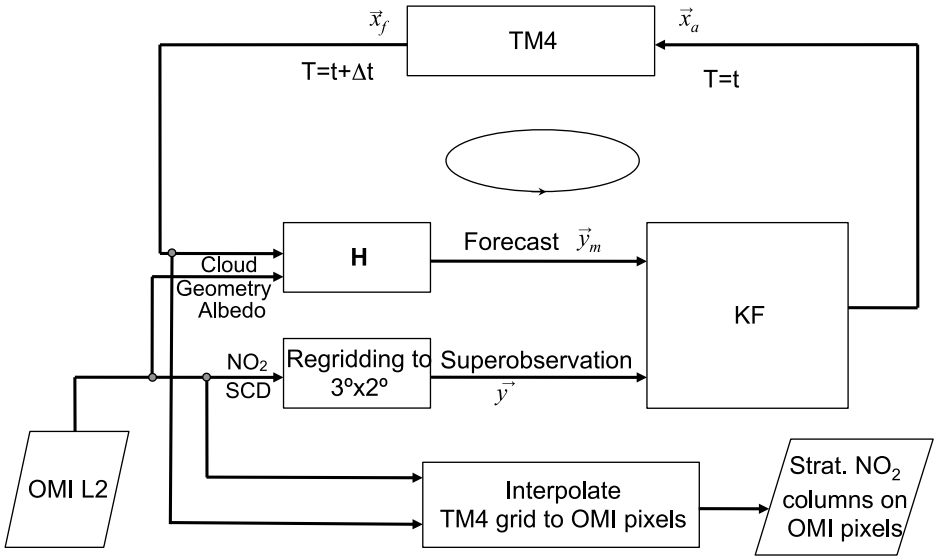

Figure 1. Schematic diagram of the OMI stratospheric NO_2 assimilation. TM4 simulates the forecast NO_2 field ($\vec{x}_f$) for the model time $t + \Delta t$ (upper branch of the scheme). OMI observations coincident with this time step are averaged over the 3° × 2° TM4 grid cells to yield superobservations $\vec{y}$. The observation operator **H** uses OMI pixel coordinates, viewing geometry, and cloud and albedo information from the OMI L2 data to convert the forecast NO_2 profiles $\vec{x}_f$ into forecast NO_2 total slant columns ($\vec{y}_m$). The Kalman filter (KF) then forces the forecast to the superobservation to produce analyzed NO_2 profiles ($\vec{x}_a$) that are input to the subsequent model time step. The stratospheric NO_2 columns for the OMI measurements result from interpolating the forecast 3° × 2° NO_2 field to the OMI pixel locations and summing the layers above the tropopause. This is represented by the lower branch.

vector and the TM4 NO_2 profile at the location of the individual OMI observations yields the slant column that would be observed by OMI given the modeled profile $\vec{x}_f$. The average of all OMI observations (and model equivalents) with center coordinates inside a 3° × 2° TM4 grid cell is treated as a single measurement, dubbed superobservation (and model equivalent). $\vec{y}_m$ is the model forecast of the superobservations, given by $\mathbf{H}\vec{x}_f$. In order to reduce the computational effort, the Kalman filter is applied for these superobservations.

[14] The diagonal elements of the observation error covariance matrix **R** equal the square of the observation error $\mathbf{R}_{ii} = \sigma_o^2$, where σ_o is chosen to depend explicitly on the modeled profile shape,

$$\sigma_o = \left(AS_{trop} + BS_{strat}\right)/S, \tag{2}$$

with S_{trop} the tropospheric contribution to the total slant column S, and S_{strat} the stratospheric contribution to the slant column taken from the TM4 forecast. The unknown true S_{trop} and S_{strat} are approximated by the model estimates. The values assigned to the coefficients A and B are 4.0 and 0.25 ($\times 10^{15}$ molecules/cm^2), respectively. This implies that the observation error rapidly increases for modeled tropospheric vertical columns larger than approximately 0.5×10^{15} molecules/cm^2. Furthermore, the small value of the stratospheric observation error B reflects the relatively accurate measurement of stratospheric NO_2; radiative transfer calculations have small errors for NO_2 in the middle and higher atmosphere. Because of averaging of OMI observations into superobservations, much of the noise in the OMI observations cancels out, consistent with our small value for B. The value of B is furthermore consistent with the standard deviation of the observed O − F value. The large value of A reflects the large retrieval uncertainty for tropospheric NO_2, which is very sensitive to assumptions on cloud modeling, surface reflectivity, profile shape or aerosol concentration [*Boersma et al.*, 2004]. In the stratosphere total reactive nitrogen (NO_y) is a well-conserved quantity, with relatively small source and sink contributions. This implies that the information from the observations can be stored in the model over long time periods. Furthermore, experiences with ozone assimilation have shown that modern weather prediction models are well capable of describing the dynamical variability of stratospheric tracer concentrations [*Eskes et al.*, 2003]. A successful stratospheric assimilation can therefore be expected. In contrast, the tropospheric NO_2 budget is characterized by strong sources and sinks, resulting in short NO_2 lifetimes of 5–20 h in the lower troposphere. Updates brought to the simulated tropospheric NO_2 concentration field are therefore rapidly lost, typically within 1 day. The observation error covariance matrix **R** defined in this way effectively filters out OMI observations with increased tropospheric NO_2 columns by attributing less weight to OMI observations over (known) polluted areas. This filtering leads to a strong forcing of the simulated stratospheric NO_2 concentrations toward the OMI observations, and will result in only a marginal adjustment of the simulated tropospheric NO_2 field.

[15] The covariance matrix **P** accounts for the forecast error due to model imperfections. The diagonal or variance is set to a fixed value $\mathbf{P}_{ii} = \sigma_f^2$, where $\sigma_f = 0.15 \times 10^{15}$ molecules/cm^2. This value is consistent with the variance of O − F values apparent over remote areas. A

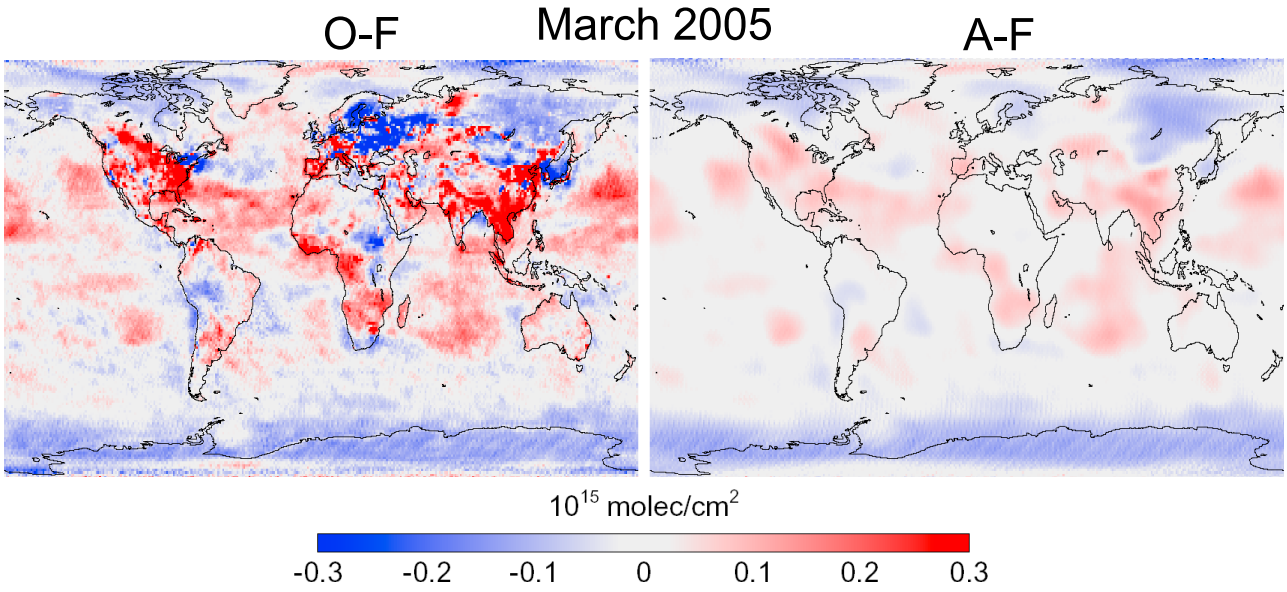

Figure 2. (left) Monthly mean observation-forecast (O − F) and (right) analysis-forecast (A − F) differences in NO_2 slant columns for March 2005 (1° × 1°). For each OMI pixel, the measured slant column (observation) and the model-predicted slant column (forecast) were divided by the same geometrical air mass factor.

second-order autoregressive (Thiebaux) function with a characteristic length of 600 km (hereafter called correlation length) describes the correlation between the errors of neighboring grid cells. This correlation length transforms a local O − F difference into a spatially extended, smeared forcing in model space. Consequently, the correlation length filters out structures smaller than 600 km in the O − F, reducing the local impact of small-scale structures (partly from tropospheric origin) on the assimilated stratospheric NO_2 field. This implies that small-scale variations in the OMI observations, such as the stripes [*Boersma et al.*, 2007], are dampened and have only minor implications for the (stratospheric) analysis. Strong gradients in stratospheric NO_2 are occasionally found, in particular related to the Noxon cliff [*Noxon*, 1979]. Such sharp drops in NO_x concentrations indicate that air masses on either side of the cliff have a very different chemical history. Error correlations are assumed to be small in such cases. To account for this we introduce an NO_2 concentration gradient dependence in the correlation,

$$C_{ij} = \begin{cases} e^{-\left(\frac{\Delta\rho_{ij}}{0.5\sigma}\right)^2} & \Delta\rho_{ij} < 0.9 \\ 0 & \Delta\rho_{ij} > 0.9 \end{cases} \qquad \text{with} \quad \Delta\rho_{ij} = \left|\frac{c_i - c_j}{c_i + c_j}\right|, \tag{3}$$

with c_i and c_j the concentrations in grid cells i and j, σ the characteristic concentration length, which is set to 30%. Such a term is effective in preventing the occurrence of negative analyzed NO_2 values within the vortex. The off-diagonal elements $\mathbf{P}_{ij}$ are the product of C_{ij} and the correlation length.

[16] All the model NO_y species (NO, NO_2, NO_3, N_2O_5, HNO_4) are assumed to be fully correlated. Hence the forcing of the modeled NO_2 field is also directly applied to the other four nitrogen oxides. The (3° × 2°) forecast NO_2 field is spatially interpolated to the location of the OMI pixel center, and the stratospheric vertical column is calculated by summing all layers above the tropopause. In the calculation of the stratospheric slant column, the NO_2 amount in each layer is multiplied by the corresponding element from the observation operator before summation. This is represented by the lower branch in the scheme shown in Figure 1. The TM4 tropopause level follows from applying the WMO 1985 definition (lowest level where the lapse rate is smaller than 2°C/km) to the ECMWF temperature profiles. The forecast stratospheric NO_2 slant columns are used in the retrieval of the tropospheric vertical column, and they are stored in the DOMINO data file (as data field "AssimilatedStratosphericSlantColumn"). The forecast stratospheric NO_2 vertical columns (data field "AssimilatedStratosphericVerticalColumn") are used in the remainder of this study. The forecast columns in regions with negligible overlap between consecutive OMI orbits, have evolved freely for about 24 model hours since previous OMI overpass and model forcing. Using forecast columns instead of the analyzed columns has the advantage of reducing attribution errors for localized tropospheric contributions to the NO_2 slant column that are not simulated by the model, for instance from boreal fires. Such events may be partly attributed to the stratosphere in the analysis, which would lead to a local underestimation of the tropospheric column.

2.2.2. Assimilation Results

[17] Figure 2 shows the global distribution of monthly mean observation minus forecast (O − F) and the model forcing (analysis minus forecast, A − F) for March 2005. The difference between Figure 2 (left) and Figure 2 (right) illustrates the effect of the assimilation: considerable O − F differences, resulting mostly from (anthropogenic) tropospheric NO_2 sources, have only a minor influence on the analysis. On the other hand, synoptic-scale structures in

O − F persist in the A − F differences. That the A − F differences are much smaller (generally less than $\pm 0.15 \times 10^{15}$ molecules/cm^2) than the O − F differences (up to $\pm 0.4 \times 10^{15}$ molecules/cm^2) demonstrates that most tropospheric contributions are effectively discounted by the assimilation procedure in combination with equation (2). The persistent synoptic-scale structures in the A − F differences indicate a slight tendency in TM4 to deviate from the observed fields. The absence of land-sea transitions in the A − F differences illustrates that the strength of the forcing is comparable over land and over sea. This reflects that the stratospheric NO_2 field is largely decoupled from the troposphere in the analysis, and as such is not bound to the geographical distribution of land-sea masses.

[18] We evaluate the impact of the assimilation by comparing a 12 month TM4 free run to the assimilation run. Both runs were initialized with the same model start field for 1 January 2005. In the tropics (30°S–30°N) the difference assimilation minus free model run increases by approximately $+0.5 \times 10^{15}$ molecules/cm^2 per month and stabilizes at $+1.3 \times 10^{15}$ molecules/cm^2, which implies that TM4 in the free-running mode underestimates the stratospheric NO_2 vertical column in the tropics by 50%. For midlatitudes the difference between TM4 and assimilation varies with season, with an amplitude comparable to the value in the tropics. The main source of stratospheric NO_2, nitrous oxide (N_2O), is not modeled by TM4, which may explain part of the biases in TM4 NO_2. Stratospheric NO_2 is effectively driven by the UARS ratio of HNO_3:O_3 in combination with the Fortuin & Kelder O_3 climatology. Since the nudging is relatively slow (the relaxation time is 2 months, comparable with the time scale of poleward transport) stratospheric NO_2 concentrations in TM4 follow the climatologies with significant delay. Imposing the HNO_3:O_3 ratio, such as applied in the original TM4 model, is likely to reduce the bias.

[19] Up to now, no validation studies of TM4 stratospheric tracers have been reported, but TM4 stratospheric ozone columns are consistent with the 30 year data record of total column ozone observations by TOMS, SBUV, GOME, SCIAMACHY, OMI and GOME-2 that is presented by *van der A et al.* [2010]. The significant differences between TM4 and assimilated stratospheric NO_2 that we find here, illustrate that the absolute values of the DOMINO stratospheric NO_2 columns are strongly driven by the OMI NO_2 observations and that the model input is limited to providing a forecast from observation-based analyzed fields.

2.3. NASA GSFC (Standard Product) Retrieval

[20] The Standard Product (SP) is an operational algorithm for the retrieval of tropospheric NO_2 vertical column densities for OMI. Analogously to the DOMINO product, the SP algorithm starts with DOAS fitted slant column densities of the OMI L2 data. The basic algorithm for the retrieval of total vertical column and tropospheric NO_2 is described by *Boersma et al.* [2002] and *Bucsela et al.* [2006]. The Standard Product identifies the stratospheric NO_2 vertical columns as the slowly varying part of the total vertical column NO_2 field, which implies that medium-scale variations up to several 100 km in the total column NO_2 field are attributed to tropospheric signals.

[21] In the first step, NO_2 slant columns are converted into initial vertical columns ($VCD_{init,SP}$) by dividing by an (unpolluted) air mass factor ($AMF_{init,SP}$). These air mass factors are derived from radiative transfer calculations with the TOMRAD radiative transfer model [*Dave*, 1965] with annually averaged simulated NO_2 profile shapes. These profiles are constructed by merging the GSFC CTM [*Douglass et al.*, 2003] 3-D profiles for the stratosphere with 3-D tropospheric profiles from the GEOS-Chem model [*Martin et al.*, 2002a].

[22] In essence the Standard Product builds on the reference sector method [*Martin et al.*, 2002b] and on the method reported by *Wenig et al.* [2003], who assumed GOME observations over unpolluted regions (oceans) to represent the stratospheric NO_2 field for these latitudes, and interpolated to fill the gaps over the continents. The Standard Product applies a second-order Fourier (wave-2) fit in 1°-wide latitude bands in the zonal direction to all data collected within ±12 h of the target orbit [*Bucsela et al.*, 2008]. Prior to the wave-2 fit, regions with known high-tropospheric NO_2 abundances (identified using GEOS-Chem) are masked and a 9° wide boxcar running average is applied in the meridional direction. Areas with strong deviations from the wave-2 fit are identified as contaminated by tropospheric NO_2 pollution and also masked. Then, the wave-2 fit is performed for the second time. The local stratospheric NO_2 column is thus based on a spatial fit to a 24 h ensemble of OMI observations, and is subtracted from the OMI observations to produce the tropospheric slant column field. The stratospheric NO_2 columns used in this study are calculated by evaluating the wave-2 polynomial, using the coefficients that are stored in the SP data file. A detailed discussion of the Standard Product algorithm can be found elsewhere [*Bucsela et al.*, 2006; *Celarier et al.*, 2008].

3. Data Sets

[23] OMI stratospheric NO_2 columns are compared to ground-based UV-Vis and FTIR measurements taken at various NDACC (Network for the Detection of Atmospheric Composition Change) stations. Part of the NDACC UV-Vis instruments belong to the SAOZ network. The nearly identical SAOZ instruments all are operated by CNRS. In this study we make a distinction between the SAOZ instruments and the other NDACC-certified UV-Vis instruments that are operated by individual institutes.

3.1. SAOZ

[24] The SAOZ (Système d'Analyse par Observations Zénithal) system constitutes a network of ground-based UV-Vis spectrometers to measure stratospheric ozone and NO_2. SAOZ spectrometers [*Pommereau and Goutail*, 1988] record the zenith sky spectrum between 300 and 620 nm at 1 nm resolution. Currently, the SAOZ network consists of 10 instruments located at various latitudes between 70°S and 70°N, and their locations are shown in Figure 3. In general, the SAOZ instruments are situated at pristine or elevated locations, far away from significant sources of tropospheric NO_2.

[25] Measurements are performed around twilight (solar zenith angles between 86° and 91°). The long light path through the stratosphere, and the relatively short vertical light path through the troposphere make the measured slant

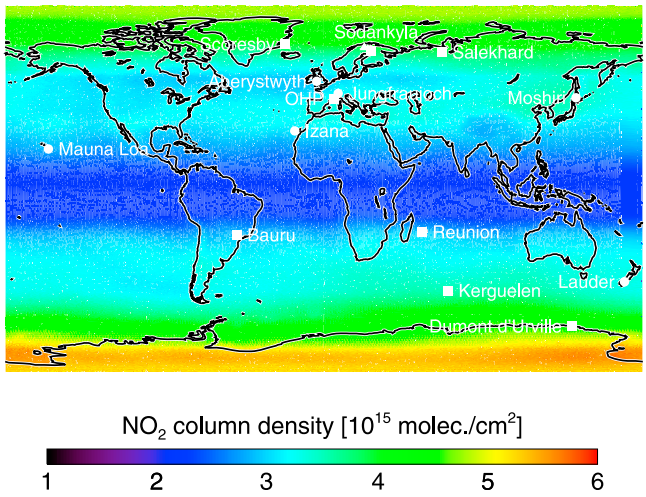

Figure 3. Geographical distribution of 14 ground-based measurement sites for remote sensing observations of stratospheric NO_2 used in this study. Squares indicate CNRS-operated SAOZ stations, circles indicate NDACC-operated stations, and the triangle indicates the FTIR station in Kiruna. The collocated FTIR stations in Izaña and Jungfraujoch are not indicated separately. The colored map represents the annual mean of DOMINO stratospheric NO_2 for 2005.

column roughly 18 times more sensitive to stratospheric NO_2 than to NO_2 in the troposphere.

[26] NO_2 slant columns are retrieved by a DOAS fit in the 410–530 nm wavelength range to the ratio of the twilight spectrum and a reference spectrum, typically taken at noon under cloud free conditions. Different SAOZ groups take different approaches for the reference spectrum. For instance, *Vaughan et al.* [2006] use a new reference spectrum for each month, whereas *Ionov et al.* [2008] employ a fixed reference spectrum for the entire measurement series at a measurement site. Slant columns are converted to vertical columns by the air mass factor (AMF) which is calculated with a radiative transfer model developed by CNRS [*Sarkissian et al.*, 1995]. The air mass factors are calculated at 470 nm taking into account solar zenith angle and NO_2 profile shape. SAOZ uses fixed AMFs for three different geographical regions: midlatitude (OHP and Kerguelen), tropics (Reunion and Bauru) and polar (Dumont d'Urville, Sodankyla, Scoresby). These AMFs have been calculated for summer sunset conditions using composite NO_2 profiles from SAGE-II, POAM-III and SAOZ balloon observations.

[27] Intercomparisons of NDACC-certified UV-Vis instruments show that retrieved NO_2 slant columns agree within 5–10% for common spectral ranges and analysis parameters, [e.g., *Vaughan et al.*; 1997; *Roscoe et al.*, 1999; *Vandaele et al.*, 2005]. However, the accuracy of the stratospheric NO_2 vertical column is limited by errors in the AMF calculation, errors in the residual NO_2 amount in the reference spectrum, and errors resulting from not accounting for the temperature dependence of the NO_2 absorption cross section. This yields an overall accuracy of 21% of stratospheric NO_2 vertical columns retrieved with ground-based UV-Vis instruments [*Ionov et al.*, 2008].

[28] In order to compare stratospheric NO_2 observations from SAOZ (sunrise, sunset) and OMI (approximately 1340 LT), we need to account for the considerable time difference between the two measurement methods. A chemical box model [*Denis et al.*, 2005; *Ionov et al.*, 2008], based on chemistry from the SLIMCAT 3-D CTM [*Chipperfield et al.*, 1996], is used to calculate representative overhead columns at 1200 LT from the SAOZ twilight measurements. This model simulates the diurnal variation of stratospheric NO_2 with 1 min time steps, and it includes 98 chemical and 39 photochemical reactions, including heterogeneous chemistry on liquid and solid aerosols. The error associated with this model-based adjustment is not included in the above quoted 21% accuracy. OMI stratospheric NO_2 data are also adjusted to local noon with the same model. The magnitude of the adjustment depends, apart from time of overpass, on season and latitude. For the SAOZ sunrise to noon correction the adjustment ranges from $<0.1 \times 10^{15}$ molecules/cm^2 (5%) in the tropics to $>2 \times 10^{15}$ molecules/cm^2 (30%) for the high-latitude stations in summer. For DOMINO the adjustment to local noon is typically smaller (up to 0.4×10^{15} molecules/cm^2, or 12%).

3.2. NDACC UV-Vis Zenith Sky Data

[29] In addition to the SAOZ stations several independently operated SAOZ-like instruments contribute to the NDACC network (http://www.ndsc.ncep.noaa.gov/). Similar to the SAOZ stations these instruments record the UV-Vis zenith sky spectrum at sunrise and sunset. NDACC and SAOZ instruments are comparable, but not identical. The operational wavelength range or the employed fitting window for NO_2 retrieval is different for some of the NDACC instruments. Furthermore, different radiative transfer codes are used to determine the AMFs. The resulting error budget has been reported to be similar to the SAOZ instruments, with a 21% accuracy of the stratospheric vertical NO_2 column [*Ionov et al.*, 2008]. The twilight NO_2 columns retrieved by the NDACC instruments are adjusted to local noon columns by the same model that was used to adjust the SAOZ and OMI measurements.

3.3. Ground-Based FTIR Stations

[30] The NDACC network also contains several NO_2 observing Fourier Transform Infra-Red (FTIR) instruments. The direct Sun measurement from FTIR is only possible at daytime under clear sky conditions. Owing to its wavelength range and high spectral resolution the FTIR method is sensitive to the pressure and temperature dependence of the NO_2 cross-section spectrum. *Camy-Peyret et al.* [1983] and *Flaud et al.* [1983] presented error estimates of FTIR NO_2 column retrievals, showing accuracies of approximately 10%. However, the dominant error source in FTIR are inaccuracies in the a priori NO_2 profile assumed in the retrieval and these can result in errors of approximately 30% [*Rinsland et al.*, 2003] as we will discuss later. Other sources of error are the assumed temperature profile, signal to noise, and the accuracy of the absorption cross section.

4. Evaluation of OMI Stratospheric NO_2

4.1. Evaluation of Ground-Based Techniques

[31] First we investigate the consistency between the FTIR and UV-Vis measurements of stratospheric NO_2. This is motivated by an earlier study by *Vaughan et al.* [1997]

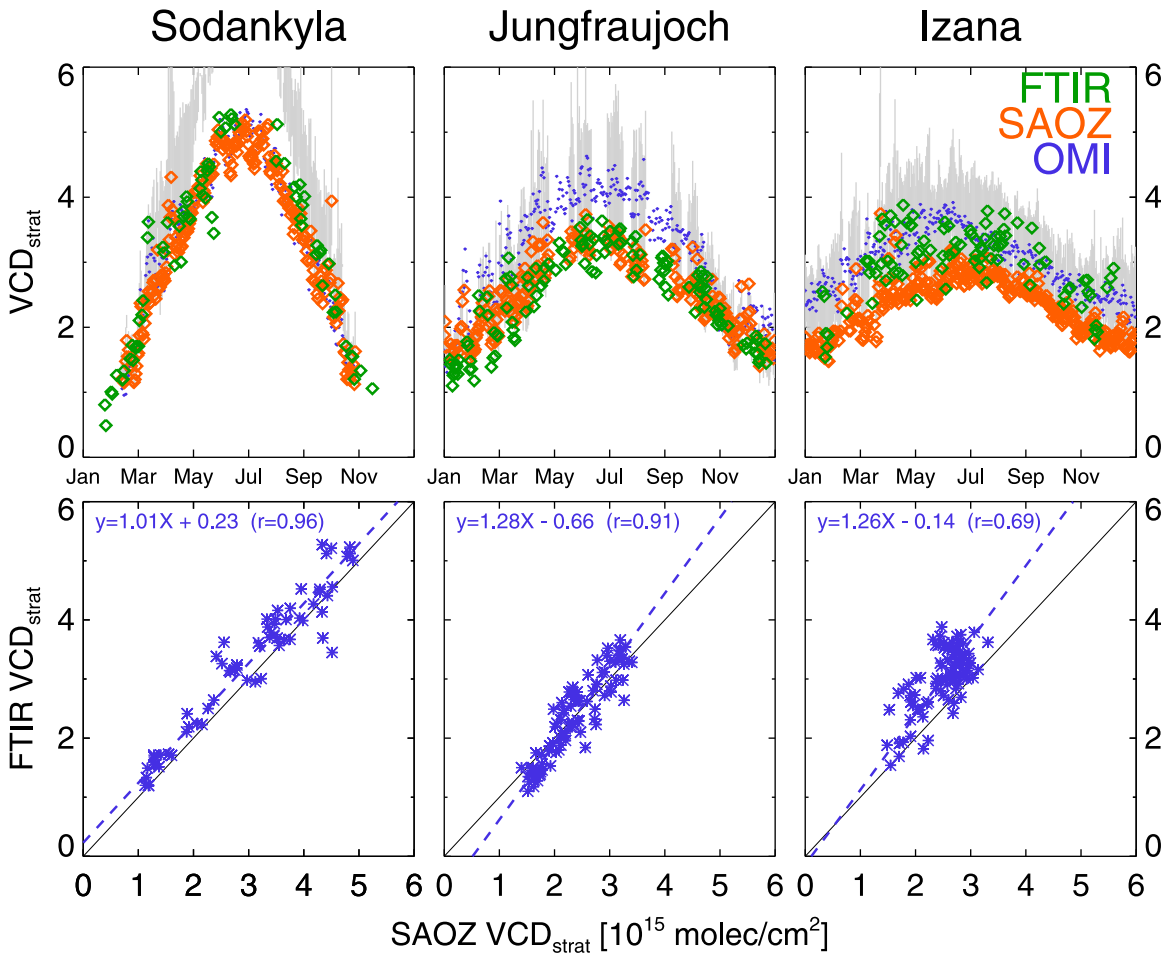

Figure 4. Comparison between SAOZ, FTIR, and DOMINO stratospheric NO_2 columns for (left) Sodankyla/Kiruna, (middle) Jungfraujoch, and (right) Izaña. OMI pixels within 10 km of the measurement station have been used. SAOZ and OMI data have been adjusted to local noon using a SLIMCAT-based chemical box model. For days with multiple FTIR measurements, the data closest in time to OMI overpass are taken, with a typical time difference between OMI overpass and FTIR measurement of 30 min to 2 h. (top) The grey bands represent the range covered by the SAOZ sunrise and sunset measurements. (bottom) The solid line in the scatterplots denotes unity, and the dashed lines represent a reduced major axis fit [*Clarke*, 1980] to the data.

that reported discrepancies of up to 30% in the NO_2 column between different UV-Vis instruments. At the NDACC stations Jungfraujoch and Izaña, FTIR instruments are collocated with zenith sky observing instruments, which enables the evaluation of both techniques against each other. The Kiruna station is located 300 km west of Sodankyla, close enough to compare the Kiruna FTIR to the Sodankyla SAOZ instrument in absence of strong gradients in stratospheric NO_2. Figure 4 shows a comparison of stratospheric NO_2 columns inferred from ground-based FTIR and UV-Vis instruments with those retrieved from OMI for Sodankyla, Jungfraujoch and Izaña. The FTIR measurement closest in time to the OMI overpass was used, and the time difference ranges from 30 min to 2 h. The time series in Figure 4 (top) show how the amplitude of the seasonal cycle increases with latitude, with the largest stratospheric NO_2 columns over Sodankyla (67.4°N) in summer. This reflects the larger number of sunlit hours at high latitudes, that causes the complete conversion of the N_2O_5 reservoir specie to NO_x in summer [*Solomon and Keys*, 1992]. The 1200 LT adjusted SAOZ data are always at the lower end of the grey bars that indicate measurements of stratospheric NO_2 at sunrise and sunset. In the summer months, the SAOZ sunrise measurements over Sodankyla are well above the adjusted noon values, for the same reason (N_2O_5 depletion).

[32] The scatterplots in Figure 4 (bottom) show that over Sodankyla the agreement between SAOZ and FTIR (and DOMINO) is very good (r = 0.96, slope = +1.01, offset = +0.23 × 10^{15} molecules/cm^2). Over Jungfraujoch we find good agreement between UV-Vis and FTIR (r = 0.91, slope = +1.28, offset = −0.66 × 10^{15} molecules/cm^2), but only after careful inspection of the effect of the a priori profile in the retrieved columns. The original a priori profile was replaced with a profile taken from the AFGL standard midlatitude atmosphere [*Anderson et al.*, 1986] that has less NO_2 in the troposphere, reducing the retrieved NO_2 columns by 30% (P. Demoulin, personal communication, 2010). Over Izaña the FTIR data are consistently higher than the zenith sky

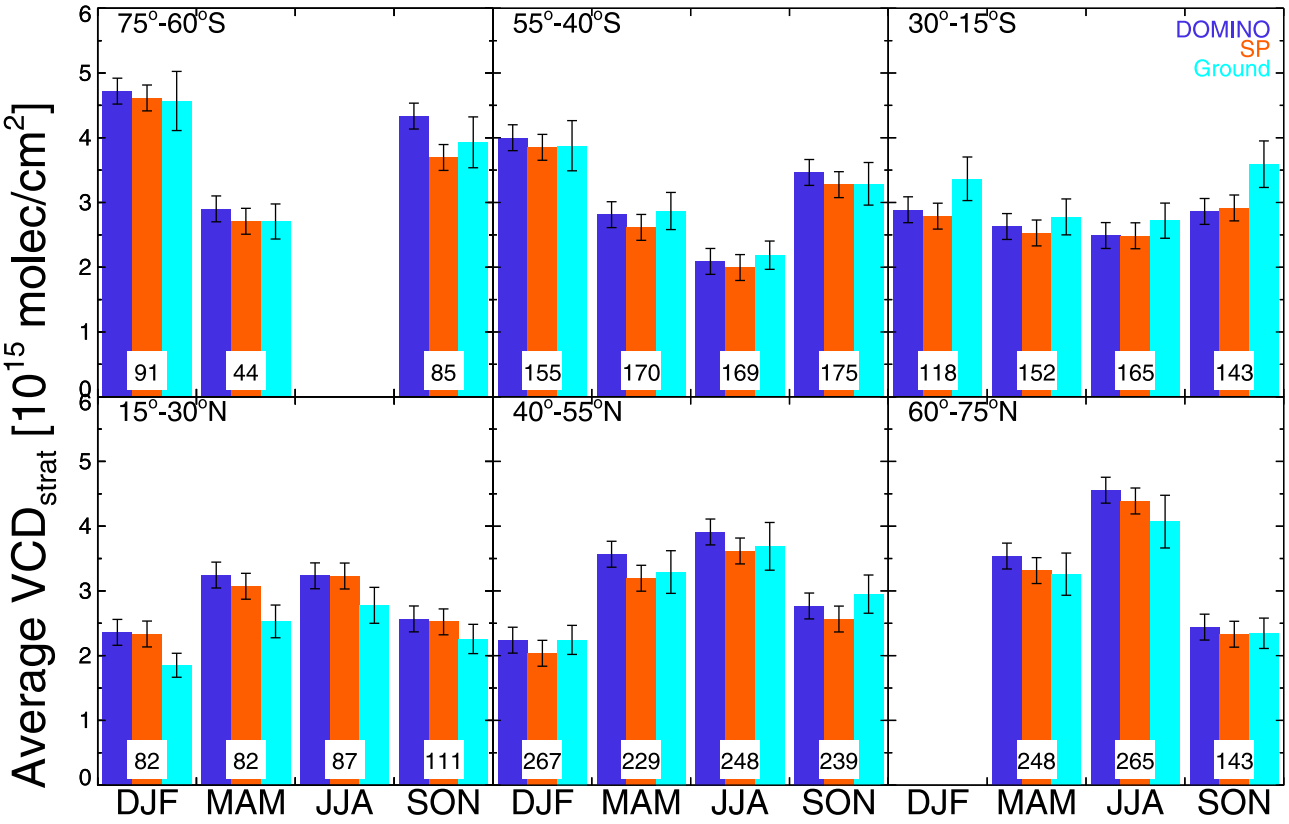

Figure 5. Comparison of DOMINO (blue), SP (red), and ground-based (cyan) stratospheric NO_2 observations as a function of season in 2005. Coincident and collocated (<10 km) OMI measurement data were adjusted to local noon. For days with multiple OMI overpasses, the overpass closest to local noon was selected. The numbers in the bars represent the number of ground-based observations contributing to the plot. The error bars give an indication of the measurement precision (0.1×10^{15} molecules/cm^2 for DOMINO and SP, 10% for the ground-based data). Bauru (22.3°S) data between 15 September to 31 January have been excluded because these are affected by high tropospheric NO_2 concentrations from biomass burning.

values with poorer correlation (r = 0.69, slope = +1.26, offset = -0.14×10^{15} molecules/cm^2). Recently, a thorough inspection of the UV-Vis instrument at Izaña revealed improper illumination of the detector and issues with the stray light correction resulting in a 15% underestimation of the UV-Vis stratospheric NO_2 columns (M. Gil, personal communication, 2010). Correcting for these inaccuracies would bring UV-Vis more in line with FTIR and OMI. We conclude that the ground-based techniques are mutually consistent within 15–20%, which is consistent with accuracies reported in other studies. *De Mazière et al.* [1998] found a +5% offset between the ground-based FTIR and zenith sky measured vertical NO_2 columns at Jungfraujoch. *Kerzenmacher et al.* [2008] performed a comprehensive validation study of ACE-FTS (a spaceborne FTIR recording solar occultation spectra) versus ground-based FTIR and UV-Vis (SAOZ) instruments and found a +15% offset between the spaceborne FTIR and SAOZ techniques.

4.2. Evaluation of OMI Stratospheric NO_2 With Ground-Based Measurements

[33] DOMINO and ground-based observations of stratospheric NO_2 over Sodankyla agree very well, as shown in Figure 4. Figure 5 shows the seasonal variation in stratospheric NO_2 columns measured by DOMINO, the Standard Product (SP) and ground-based instruments from the NDACC network, with high-NO_2 columns in summer and smaller columns in winter. DOMINO and SP both show reasonable agreement with the ground-based data. The bias between the latitude and seasonally averaged OMI products and ground-based data is generally within 1×10^{15} molecules/cm^2, and as shown in Figure 6, the stations do not share a clear persistent bias pattern. Figure 6 shows the differences between OMI and ground-based measurements of stratospheric NO_2 at individual stations. Figure 6 does not reveal a consistent seasonal cycle in the bias among the stations. Table 1 shows that, with the exception of Dumont d'Urville, the average bias for a given station for both retrievals is smaller than 0.3×10^{15} molecules/cm^2, with an RMS error of approximately 0.4×10^{15} molecules/cm^2. The agreement between OMI and ground-based stratospheric NO_2 is on average within 13%. We consider this agreement optimal, given the estimated accuracy of the ground-based techniques of 21% and the precision of the OMI retrievals of approximately 0.2×10^{15} molecules/cm^2. Over the SAOZ and NDACC stations, DOMINO exceeds ground-based stratospheric NO_2 by $+0.23 \times 10^{15}$ molecules/cm^2 and SP by $+0.06 \times 10^{15}$ molecules/cm^2 which implies that DOMINO is

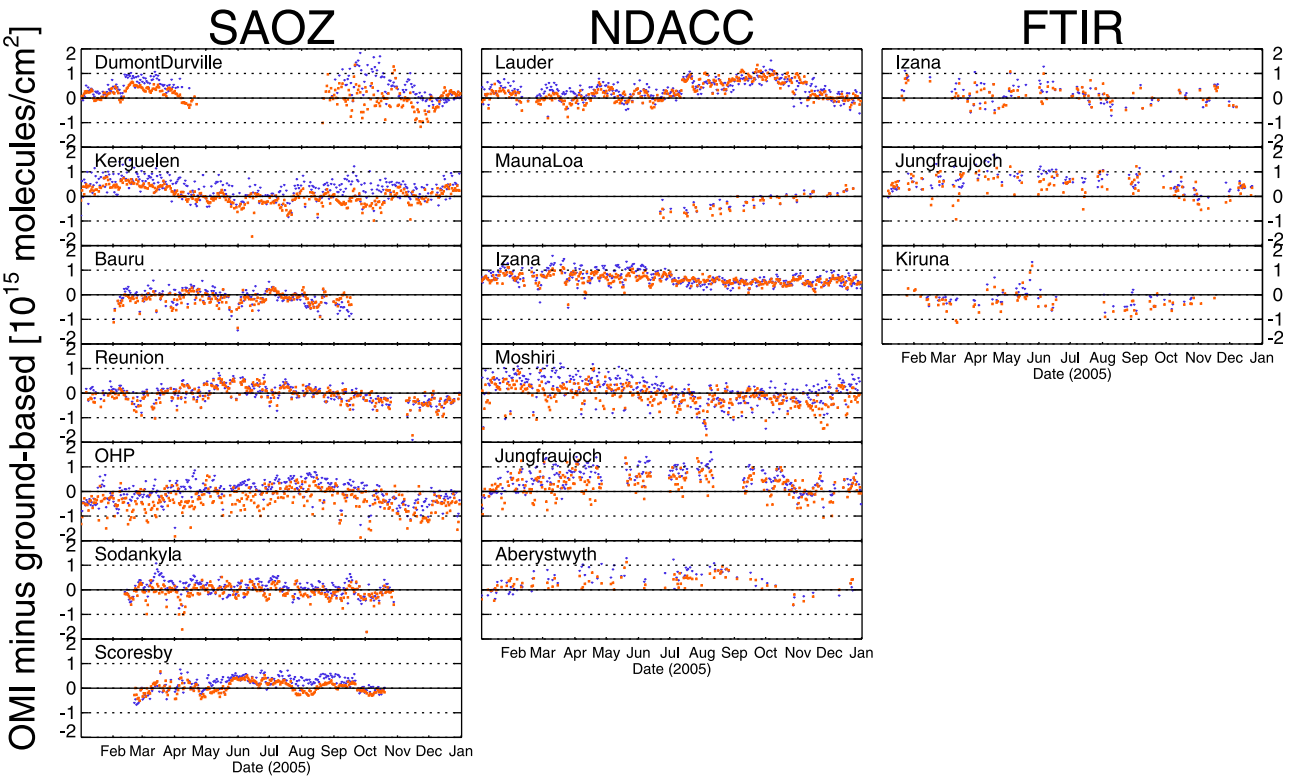

Figure 6. Differences between OMI stratospheric NO_2 columns and ground-based observations for various stations in 2005. Blue dots indicate the differences between DOMINO and ground-based stratospheric NO_2, and red dots represent SP minus ground-based. Only satellite observations within 10 km of the ground-based station have been selected, and ground-based and satellite data have been adjusted to 1200 local time (LT). In case of multiple OMI overpasses per day, the overpass closest to local noon was selected.

Table 1. Statistical Summary of Comparison DOMINO and SP Versus Ground-Based Observations

Station	Absolute Difference		Relative Difference (%)		RMS		*r*	
	DOMINO	SP	DOMINO	SP	DOMINO	SP	DOMINO	SP
				SAOZ				
Dumont d'Urville	0.471	0.074	11.7	1.9	0.435	0.401	0.886	0.926
Kerguelen	0.338	0.024	10.6	0.8	0.399	0.369	0.886	0.894
Bauru	−0.109	−0.163	−3.4	−5.1	0.318	0.252	0.535	0.726
Reunion	−0.040	−0.084	−1.3	−2.8	0.349	0.334	0.660	0.732
OHP	−0.049	−0.381	−1.5	−11.6	0.454	0.467	0.824	0.767
Sodankyla	0.090	−0.101	2.6	−3.0	0.316	0.292	0.965	0.971
Scoresby	0.198	0.041	5.8	1.2	0.288	0.232	0.980	0.980
Mean	0.128	−0.084	3.5	−2.7	0.366	0.335	0.819	0.857
				Other NDACC				
Lauder	0.355	0.279	12.3	9.7	0.360	0.404	0.896	0.867
Mauna Loa	−0.154	−0.239	−5.5	−8.5	0.276	0.339	0.946	0.928
Izaña	0.681	0.617	29.1	26.4	0.291	0.198	0.794	0.897
Moshiri	0.137	−0.119	4.2	−3.7	0.511	0.428	0.706	0.803
Jungfraujoch	0.519	0.261	21.0	10.6	0.450	0.447	0.891	0.814
Aberystwyth	0.438	0.298	17.1	11.6	0.422	0.320	0.953	0.951
Mean	0.329	0.183	13.0	7.7	0.385	0.356	0.864	0.877
				FTIR				
Izaña	0.205	0.127	6.8	4.3	0.414	0.354	0.627	0.730
Jungfraujoch	0.619	0.424	25.3	17.3	0.355	0.411	0.929	0.859
Kiruna	−0.120	−0.272	−3.6	−8.8	0.347	0.384	0.958	0.957
Mean	0.235	0.093	9.5	4.3	0.372	0.383	0.838	0.849

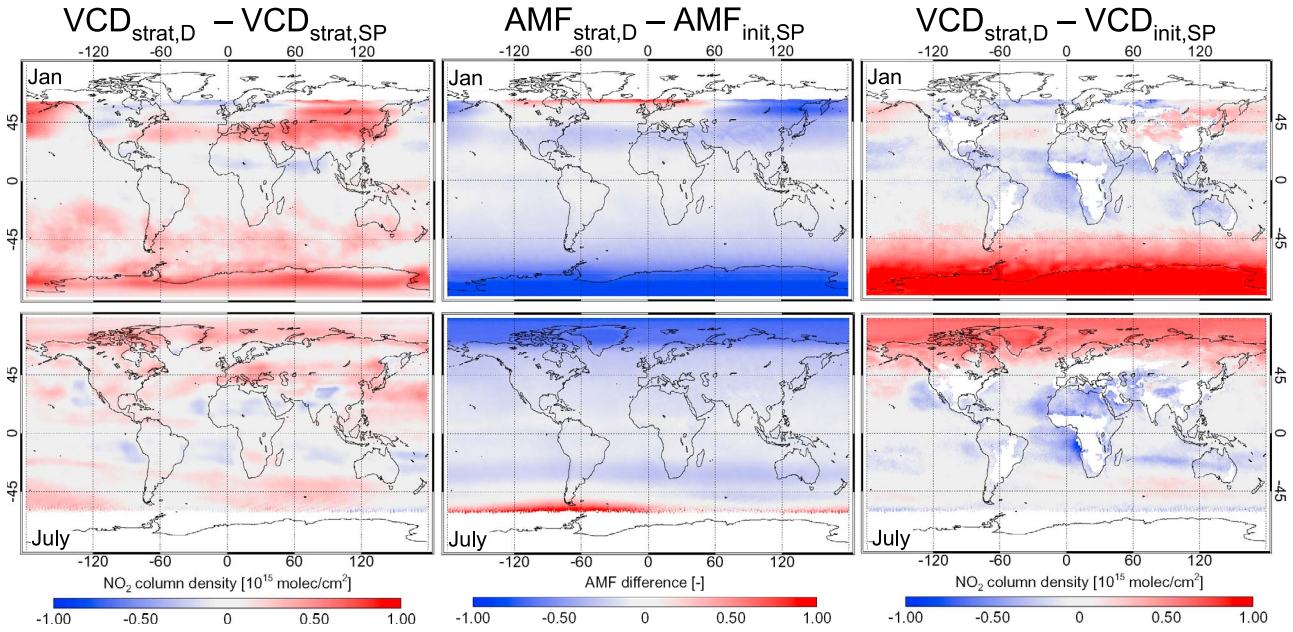

Figure 7. Comparison between DOMINO and Standard Product (SP) retrievals of stratospheric NO_2 for (top) January 2005 and (bottom) July 2005. (left) Monthly mean difference $VCD_{strat,D} - VCD_{strat,SP}$, (middle) $AMF_{strat,D} - AMF_{init,SP}$, and (right) $VCD_{strat,D} - VCD_{init,SP}$. In Figure 7 (right), regions with high tropospheric NO_2 concentrations (>1 × 10^{15} molecules/cm^2 in annual mean DOMINO) are masked.

on average approximately 0.2 × 10^{15} molecules/cm^2 higher than SP over these stations.

5. Detailed Comparison of Stratospheric NO_2 From DOMINO and SP

[34] Figures 5 and 6 show that the DOMINO stratospheric columns are higher than those from SP. This is confirmed by Table 1, which summarizes the annual mean bias between the OMI retrievals and the ground-based measurements. Figure 7 shows a comparison for DOMINO and SP stratospheric NO_2 retrievals for January and July 2005. The left panel confirms that DOMINO is generally higher than SP, more so in January than in July 2005. Figure 7 also shows that the bias between the two retrievals is not uniform, but reveals large, synoptic-scale spatial features. Such differences have been reported earlier by *Lamsal et al.* [2010], who found DOMINO and SP stratospheric slant columns to agree within ±1 × 10^{15} molecules/cm^2. The stratospheric NO_2 field retrieved from SCIAMACHY limb measurements [*Beirle et al.*, 2010] shows considerable longitudinal variation at midlatitudes, that is similar to the zonal variations in DOMINO stratospheric NO_2. This indicates that the synoptic-scale spatial features in the difference between DOMINO and SP stratospheric NO_2 result from the SP not properly capturing the longitudinal variation in the stratospheric NO_2 field. Here we examine the origin of the differences further, by comparing the stratospheric AMFs of both algorithms. Figure 7 (middle) clearly shows that DOMINO AMFs are smaller than those from the SP, especially at large solar zenith angles. This is supported by the comparison between stratospheric AMFs near the equator shown in Figure 8. For this particular part of the orbit, we find discrepancies between DOMINO and SP AMFs on the order of 5% with a notable increase around viewing zenith angles of 45°. Investigation of the look-up tables of the DOMINO and SP revealed that the latter has reference points for VZA = 0°, 30°, 45° & 70°, indicating that the large discrepancy for VZAs between 45° and 70° is most likely due to interpolation errors in the SP look-up table. In future versions, the SP look-up table will use more reference points to resolve this issue. The systematic discrepancy of approximately 5% between the AMFs for VZA < 45° result from differences in the AMF calculation between the DOMINO and SP algorithms. Table 2 gives an overview of all differences between both algorithms. Different NO_2 profile shapes (DOMINO profiles are taken from TM4 assimilation whereas Standard Product profiles are derived from merged GSFC CTM and GEOS-Chem simulations) accounts for a 1–2% difference between the DOMINO stratospheric AMF and $AMF_{init,SP}$. Similarly, the correction for the temperature sensitivity of the NO_2 spectrum discussed in section 2.2 will introduce differences as DOMINO uses ECMWF temperature profiles whereas SP uses climatological profiles. The different radiative transfer models used for the AMF calculation (DAK in case of DOMINO and TOMRAD for SP) account for another 1–2% difference in the AMFs. Both models assume plane-parallel atmospheres, however TOMRAD includes a correction for atmospheric sphericity while DAK includes polarization [*Stammes et al.*, 1989].

[35] Figure 7 (right) shows the impact of the AMF differences alone. The DOMINO stratospheric columns deviate more strongly from the SP initial vertical columns ($VCD_{init,SP}$) than the ultimately reported (wave-2 processed) SP stratospheric columns. Apparently, masking out polluted areas, accounting for tropospheric contributions to $VCD_{init,SP}$, and the wave-2 processing itself, compensate to

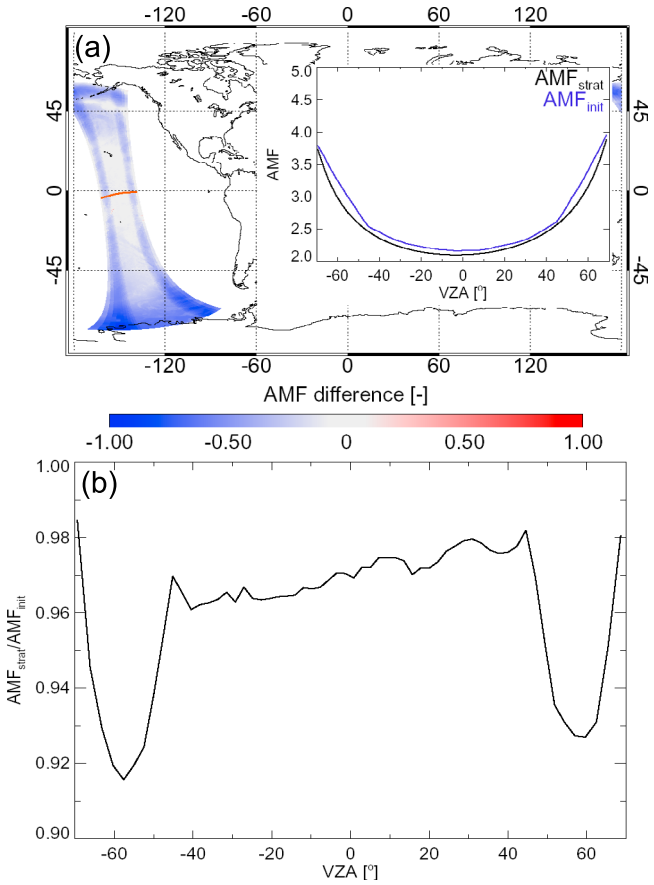

Figure 8. Comparison between stratospheric air mass factors (AMF) between DOMINO and Standard Product (SP) retrievals of stratospheric NO_2 on 23 January 2005. (a) $AMF_{strat,D} - AMF_{init,SP}$ for OMI orbit 2806 over the Pacific. The inset shows, for a single OMI measurement, the variation of $AMF_{strat,D}$ and $AMF_{init,SP}$ as a function of viewing zenith angle (VZA). The red line marks the location of the selected OMI measurement. (b) $AMF_{strat,D}/AMF_{init,SP}$ as a function of VZA. The negative viewing zenith angles correspond to the western part of the swath.

some extent for the higher SP AMFs, as indicated by the smaller differences between DOMINO and SP stratospheric NO_2 columns than between DOMINO $VCD_{strat,D}$ and SP $VCD_{init,SP}$ in Figure 7 (left).

6. Day-to-Day Dynamical Effects

[36] The Arctic polar vortex of the 2004–2005 winter was dynamically active with various excursions to lower latitudes between January and March [*Singleton et al.*, 2007]. A major stratospheric warming in mid-March caused the final breakup of the vortex [*Manney et al.*, 2006; *Singleton et al.*, 2007].

[37] Figure 9 shows the dynamic behavior of the polar vortex in the period from 9 to 21 March 2005. The PV and temperature at 50 hPa (third and fourth columns, respectively, of Figure 9) show that until 14 March the polar vortex appears stationary over the North Atlantic. On 17 March the vortex has tilted in east-west direction, after which it collapsed and broke up as seen on 21 March.

[38] The stratospheric NO_2 profile peaks between 30 and 50 hPa, and therefore we expect good spatial correlation between the DOMINO stratospheric NO_2 field (Figure 9, first column) and the temperature distribution at 50 hPa (Figure 9, third column). During 9–14 March OMI observes reduced stratospheric NO_2 columns inside the vortex over the North Atlantic and Greenland as compared to air masses outside the vortex, and enhanced NO_2 outside the vortex over Siberia and southern Europe. The boundary between reduced and enhanced stratospheric NO_2 roughly coincides with the −65°C contour at 50 hPa. On 17 March, the reduced NO_2 columns over Great Britain coincide with the low temperatures inside the tilted and weakening vortex.

[39] The synoptic-scale variations in the stratospheric NO_2 field around the vortex are not observed by the Standard Product (second column of Figure 9), but are smoothed by the wave-2 fitting instead. Actually, the enhanced stratospheric NO_2 at the vortex edge shows up as a reduction in the SP NO_2, probably resulting from the masking of polluted areas.

[40] We now focus on the effect of the movement of the vortex edge on stratospheric NO_2 over Sodankyla. Temperature and PV at 50 hPa on 9 March show that the vortex lies over Sodankyla, that is skirted by the vortex edge and the warmer air mass with enhanced stratospheric NO_2 outside the vortex. The westward displacement of the vortex on 12 March moves NO_2-rich air over Sodankyla, which results in an episodic enhancement of the stratospheric NO_2 columns of more than 1×10^{15} molecules/cm^2. Figure 10 shows DOMINO and FTIR observations over Sodankyla and Jungfraujoch of this episodic enhancement, that peaks on 14 March and lasts approximately 7 days.

[41] Figure 10 shows that the stratospheric NO_2 column over Sodankyla is coupled to the temperature at 30 hPa. The persistent low temperatures ($T \approx -80$°C) at 30 hPa in the first half of February coincide with low and unchanging FTIR-observed NO_2 columns (approximately 1×10^{15} molecules/cm^2). After 21 February the stratospheric NO_2 column increases steadily in accordance with the increasing temperature, and the episodic enhancement of stratospheric NO_2 around 15 March correlates with a

Table 2. Overview of Algorithm Differences Between OMI DOMINO and OMI SP

Algorithm	Stripe Correction	Radiative Transfer Model	Albedo		Stratospheric Column	Profile Shape
			λ (nm)	Source		
DOMINO	no	DAK	440	TOMS-GOME	TM4 assimilation	TM4 climatology of GEOS-Chem and GSFC CTM
SP	yes	TOMRAD	440	GOME	wave-2 fit	

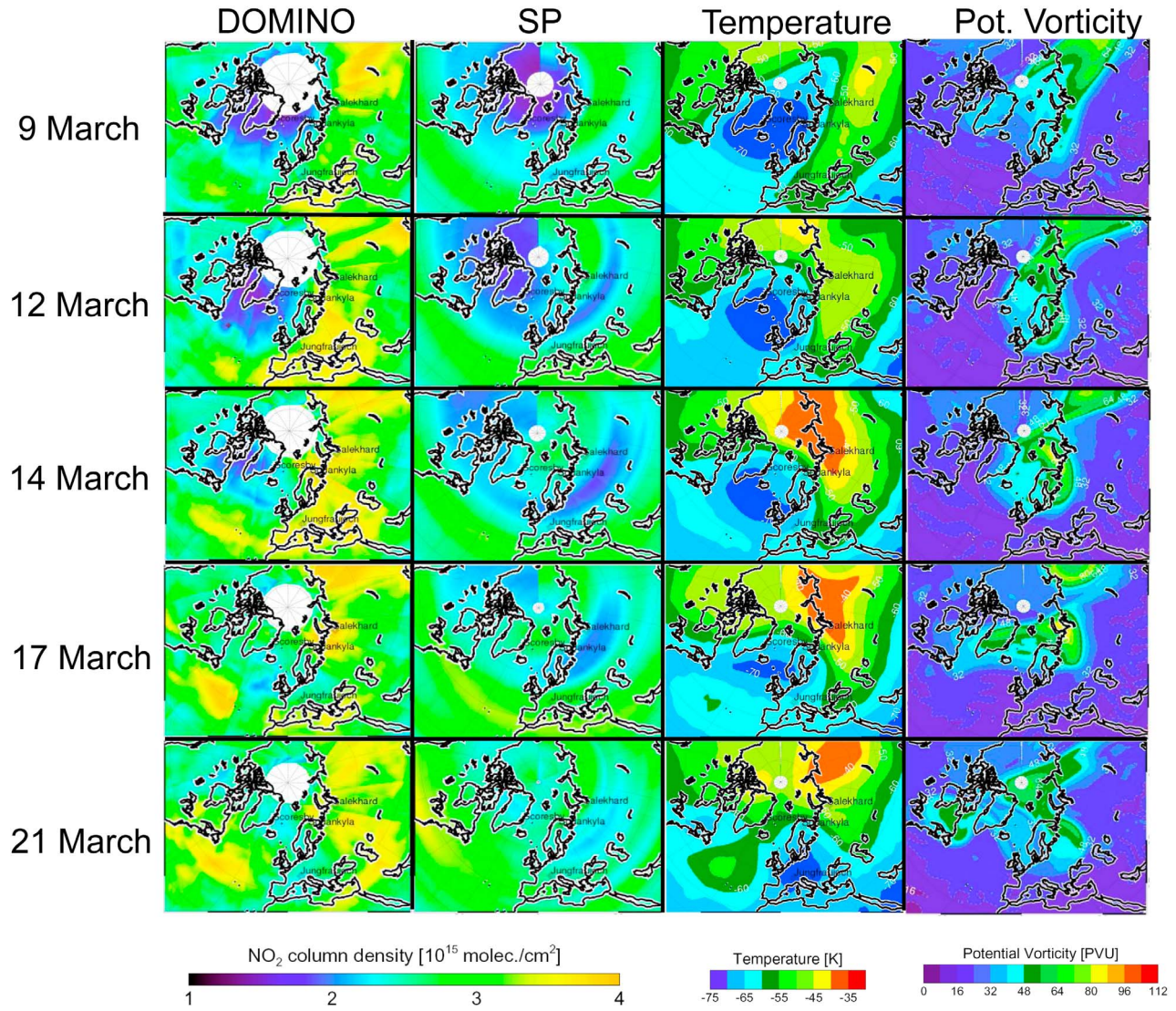

Figure 9. Time series (9, 12, 14, 17, and 21 March 2005) of polar vortex dynamics. First and second columns represent stratospheric NO_2 fields from DOMINO and SP, respectively, at local time of approximately 1330 LT. Third and fourth columns indicate the temperature and potential vorticity, respectively, at 50 hPa (1200 UTC) from ECWMF (ERA interim model version 1, analysis data).

sudden increase in the 30 hPa temperature over Sodankyla. Such positive correlations between short-term changes and local stratospheric temperature have been observed before [*Mount et al.*, 1987; *Pommereau and Goutail*, 1988]. We find a temperature dependence of $dNO_2/dT = 7 \times 10^{13}$ molecules/cm^2/K ($r = 0.95$), which is consistent with the 6×10^{13} molecules/cm^2/K over Kiruna reported by *Pommereau and Goutail* [1988]. It is unlikely that the observed temperature dependence of the stratospheric NO_2 column results from the temperature sensitivity of the NO_2 absorption cross section in the spectral fitting. First of all, the DOMINO retrieval takes this sensitivity into account (see section 2.2). Furthermore, if this sensitivity were to be neglected, it is much weaker and different in sign (−0.3%/K) than the effect we find here (+3.5%/K over Kiruna). We attribute the coupling between temperature and stratospheric NO_2 to the temperature dependence of the N_2O_5 (photo) dissociation rate and the NO_x partitioning, as proposed by *Van Roozendael et al.* [1994]. The weaker correlation between temperature and stratospheric NO_2 column over Jungfraujoch (Figure 10, top) most likely results from stronger stratospheric dynamics at this location.

[42] During the cold winter of 2004–2005, over a large area the stratospheric temperatures fell below the formation temperature of polar stratospheric clouds (PSC), resulting in increased ozone loss in the Arctic stratosphere [*Singleton et al.*, 2007]. Until 11 March the air over Sodankyla is inside the polar vortex, however after 21 February the stratospheric NO_2 column over Sodankyla increases steadily with the rising temperature at 30 hPa. This implies that the N_2O_5 and HNO_3 reservoirs in the vortex air over Sodankyla are not depleted by denitrification and subsequent sedimentation, but are still present to be (photolytically) converted into NO_x.

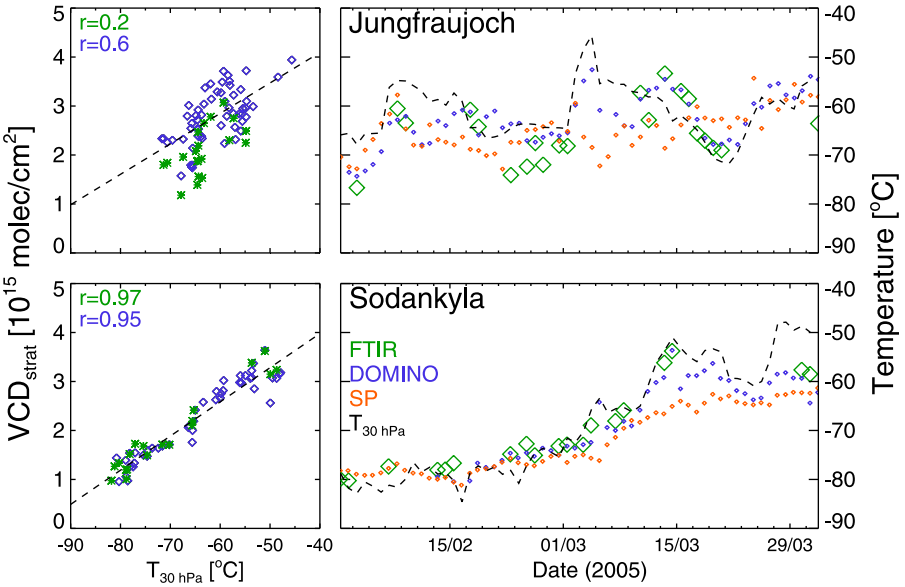

Figure 10. (right) Time series of ground-based and collocated OMI observations of stratospheric NO_2 column over (top) Jungfraujoch and (bottom) Sodankyla. OMI pixels within a 10 km radius of the ground station were selected. For multiple overpasses the OMI measurement closest to 1300 LT was used. Shown are ground-based FTIR (green diamonds), together with OMI DOMINO (blue) and OMI Standard Product (red) stratospheric NO_2 columns. The Jungfraujoch FTIR measurements were adjusted (factor: +1.23, offset: −0.125) to correct for the mismatch between FTIR and DOMINO as shown in Figure 4. The dashed line represents the ECMWF temperature at 30 hPa. (left) Scatterplots of FTIR (green) and DOMINO (blue) stratospheric NO_2 columns versus temperature for (top) Jungfraujoch and (bottom) Sodankyla. The dashed line represents a linear fit of the stratospheric NO_2 to the temperature data.

[43] Figure 10 shows that the Standard Product reproduces the seasonal trend of the stratospheric NO_2 but does not capture the short-term increases associated with the vortex displacement. This is also shown by the sequence of SP stratospheric NO_2 plots in Figure 9 (second column). Figure 10 (bottom) shows that the discrepancy between DOMINO and SP stratospheric NO_2 in case of large gradients in the stratospheric NO_2 field can be as large as 1×10^{15} molecules/cm^2.

7. OMI Observations of the Diurnal Variation of Stratospheric NO_2

[44] As a result of OMI's 2600 km wide swath, consecutive orbits start to overlap poleward of 30° latitude. The overlap increases with increasing latitude and results in up to 4 OMI overpasses per day at the same ground location near the Arctic circle. The number of overpasses is even higher for regions in midnight sun when OMI observations are also possible during the descending part ("night-side") of the orbit. For instance, Scoresby (70.5°N) can have as much as 7 OMI overpasses in summer. Therefore, OMI is able to sample the diurnal variation of stratospheric NO_2 from space with an interval of 100 min. Initial attempts to observing the diurnal variation of stratospheric NO_2 from space made use of climatological data [*Sassi and Salby*, 1999; *Brohede et al.*, 2007]. Here we report for the first time on the direct observation of the diurnal variation in stratospheric NO_2 columns. Figure 11a shows the diurnal variation of DOMINO stratospheric NO_2 over Scoresby on individual days between 9 March and 8 October 2005. With the exception of very early measurements in June and July, stratospheric NO_2 increases quasi-linearly during the day. The number of daily overpasses increases from winter to summer as a result of the increasing number of sunlit hours with season. The slope of the curves in Figure 11a indicates that the increase rate of stratospheric NO_2 is larger in spring and fall than during summer. The low increase rate in summer results from the depletion of the N_2O_5 reservoir by photodissociation during the long sunlit hours, while the nights are too short to replenish the reservoir. The DOMINO stratospheric NO_2 column over Scoresby in June–July (represented by the light and dark green lines in Figure 11a) decreases before 1000 LT (OMI measurements from the descending part of the orbit), and increases quasi-linearly after 1000 LT (OMI measurements from the ascending part of the orbit). We hypothesize that the early morning decrease is caused by the rising Sun, shifting the NO_x partitioning toward NO. The observed early morning decrease and consecutive increase after 1000 LT is consistent with SLIMCAT-based box model simulations [see, e.g., *Celarier et al.*, 2008, Figure 2]. For comparison, Figure 11b shows the diurnal variation of DOMINO stratospheric NO_2 over Jungfraujoch. Because of its lower latitude (46.5°N), Jungfraujoch has at most two OMI overpasses per day. Apart from the seasonal increase in stratospheric NO_2, we find that the increase rate is more constant throughout the year compared to the high-latitude sites. The weaker seasonal dependence of the increase rate is caused by the longer nights that allow for the replenishing of N_2O_5.

[45] Figure 12 shows the OMI-inferred (Figure 12a) and SAOZ-inferred (Figure 12b) linear increase rate of strato-

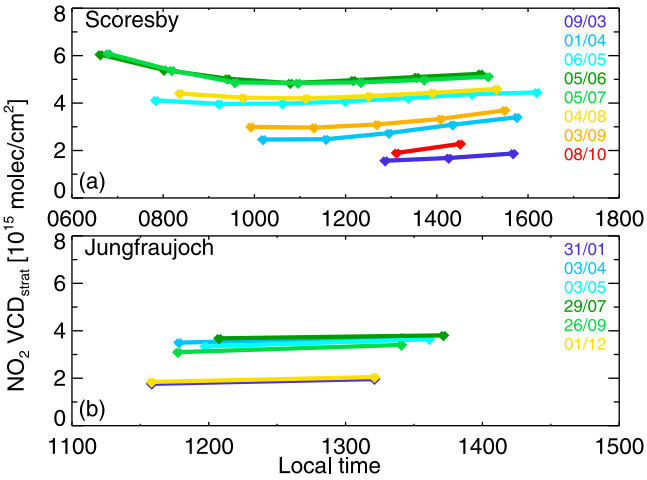

Figure 11. OMI stratospheric NO_2 column over (a) Scoresby (70.5°N, 22°W) and (b) Jungfraujoch (46.5°N, 8°E) as a function of local time of observation. The colors refer to the day and month of observation.

spheric NO_2 for Scoresby and other high-latitude SAOZ stations. The linear increase rates of stratospheric NO_2 for these high-latitude sites both show a distinct seasonal dependence, with strongest increases in spring and fall, reflecting the formation of N_2O_5 during the night in those seasons.

[46] The increase rate is determined by a linear fit to OMI stratospheric NO_2 (forecast based on assimilation) of consecutive overpasses after 1000 LT. We also determined the increase rate using the measured slant columns divided by the geometric air mass factor. The resulting increase rates were very similar to the results presented in Figure 12a as is illustrated by the coplotted slant column-based increase rates for Kiruna (solid black boxes), showing that the increase rates reported here do not follow from the assimilation, but are actually observed.

[47] At high latitudes, in spring and fall the increase rate is approximately 0.2×10^{15} molecules/cm^2/h and drops to $0.05–0.1 \times 10^{15}$ molecules/cm^2/h in summer. For Salekhard and Zhigansk (orange and red data points in Figure 12a) the OMI-inferred increase rate in spring (0.4×10^{15} molecules/cm^2/h) is considerably higher than in fall (0.15×10^{15} molecules/cm^2/h). This asymmetry between spring and fall is likely caused by the collar of NO_y-rich (and warmer) air, which girds the Arctic polar vortex, that lies over Salekhard and Zhigansk in spring. In fall, the vortex and its surrounding collar are absent. The position and movement of the Arctic polar vortex in spring 2005 was discussed in section 6. The seasonal dependence of the increase rate derived from SAOZ measurements (Figure 12b) is similar to DOMINO, with a maximum in spring and fall, and a minimum in summer. SAOZ-inferred increase rates over Salekhard also indicate a higher increase rate in spring than in fall. During summer, SAOZ-derived increase rates for high-latitude sites are close to 0, which is consistent with the identical morning and evening SAOZ NO_2 columns over Sodankyla in summer reported by *Goutail et al.* [1994]. For midlatitudes, the OMI-derived increase rates (Figure 12c) are similar to those derived from SAOZ (Figure 12d), with weak seasonal dependence. The OMI and SAOZ-inferred increase rates over Jungfraujoch are comparable to the annual mean increase rate of 0.1×10^{15} molecules/cm^2/h reported for Zugspitze [*Sussmann et al.*, 2005]. For comparison, *Gil et al.* [2008] reported an annual mean increase of 0.06×10^{15} molecules/cm^2/h over Izaña (28.3°N).

[48] Figure 13 shows a map of the mean linear increase rate of OMI stratospheric NO_2 for the Northern Hemisphere, derived for the first (Figure 13, top) and second half (Figure 13, bottom) of March 2005. The geographical distribution of the increase rate closely resembles the morphology of the stratospheric NO_2 that was presented in Figure 9: the region with low increase rates coincides with the low NO_2 values inside the denoxified polar vortex and we find high increase rates for the air outside the vortex that is rich in reactive nitrogen. The mid-March break-up of the polar vortex is reflected in the geographical distribution and the values of the increase rate for the second half of March (Figure 13, bottom): the area with low increase rates has shrunk, and the value of the increase rates themselves has grown.

8. OMI Observed Trends Stratospheric NO_2

[49] The DOMINO data set covers more than 5 years (October 2004 to May 2010) of global stratospheric and tropospheric NO_2 observations, which allows for the study of temporal variability on various time scales in stratospheric NO_2.

8.1. Seasonal Variation and QBO

[50] Figure 14 shows a multiyear time series of zonally averaged DOMINO stratospheric NO_2 columns. Over the polar and midlatitudes, stratospheric NO_2 shows a distinct annual cycle that is related to the number of sunlit hours and peaks in summer. The annual cycle is strongest over the polar regions, because of wintertime denoxification in the polar night when stratospheric NO_2 is converted into the long-lived HNO_3 and N_2O_5 reservoirs. The latitudes between 60°–90°S show reduced NO_2 columns in Antarctic spring (OND) as a result of denitrification inside the polar vortex during winter and early spring.

[51] Figure 14 shows consistently higher summertime values of stratospheric NO_2 over the Antarctic in comparison to the Arctic. This interhemispheric asymmetry in the summertime stratospheric NO_2 columns has also been observed in GOME [*Wenig et al.*, 2004] and in ODIN/OSIRIS measurements [*Brohede et al.*, 2007]. *Solomon et al.* [1984] attribute this interhemispheric asymmetry to differences in the meridional circulation as the Southern Hemisphere exhibits much less planetary wave activity than the Northern Hemisphere. The weaker planetary wave activity in the Southern Hemisphere should result in less efficient transport away from the pole. *Naudet et al.* [1987] suggested that the lower albedo (more ocean) at visible wavelengths and larger solar zenith angles in the Southern Hemisphere (resulting from the smaller Earth-Sun distance in Southern Hemisphere summer) lead to less photodissociation and thus higher concentrations of NO_2 in the stratosphere. Model calculations by *Cook and Roscoe* [2009] show that the NO_x partitioning depends on temperature, with an increase of the modeled NO_2 vertical column of

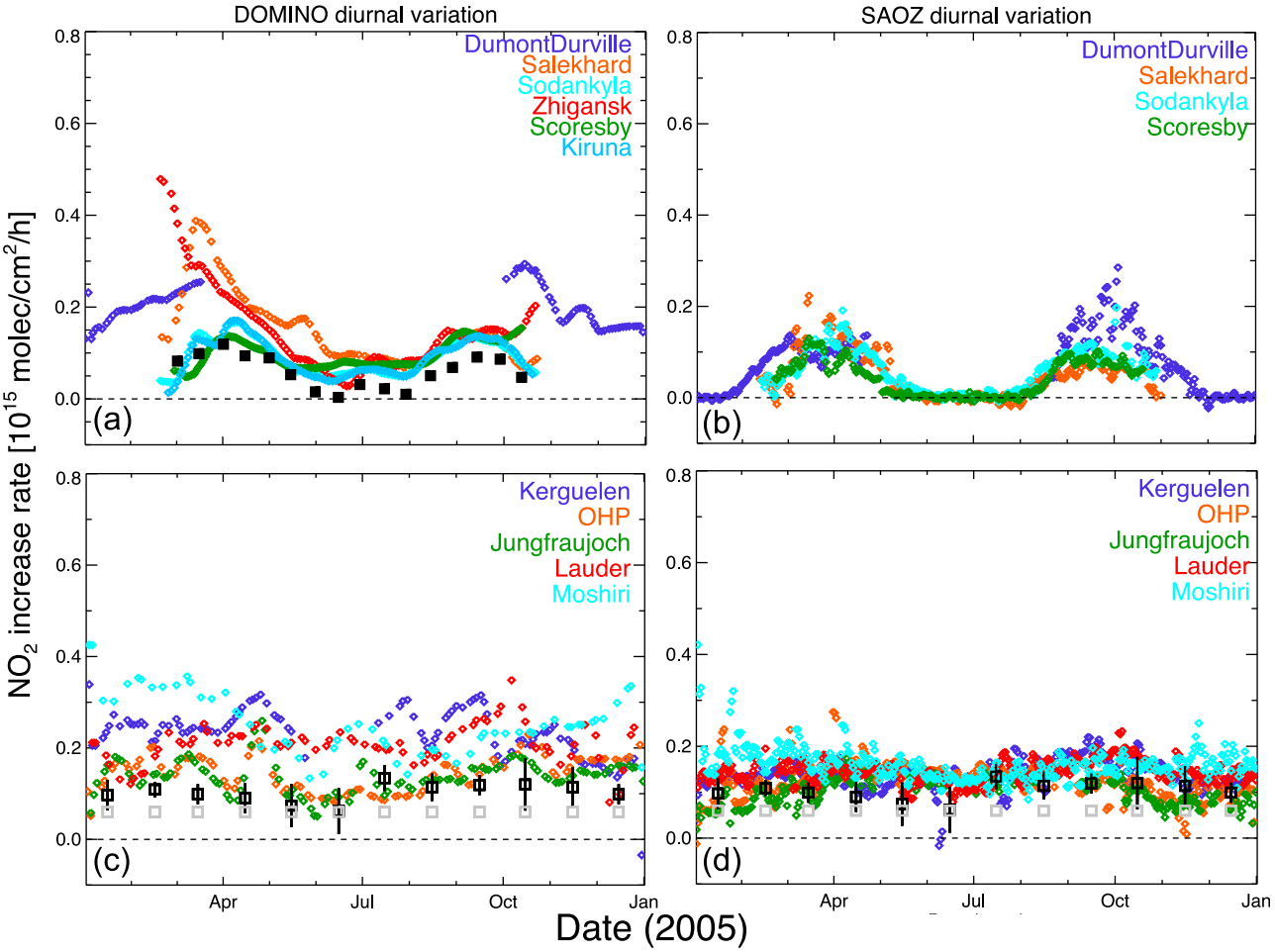

Figure 12. Increase rate of stratospheric NO_2 as a function of month for (a) seasonal variation in the increase rate of the DOMINO stratospheric NO_2 column over high-latitude stations with three or more daily overpasses. (b) Linear increase rate for high-latitude stations derived from sunrise and sunset SAOZ measurements. (c) Same as Figure 12a for midlatitude stations with two or more daily overpasses. (d) Same as Figure 12b for midlatitude stations. The OMI increase rate follows from a linear fit to the observations performed during the ascending part (when the spacecraft flies northward) of consecutive orbits. Curves in Figures 12a and 12c were smoothed by a nine-point median filter followed by 15 day averaging; curves in Figures 12b and 12d were smoothed by 3 day averaging. The solid boxes in Figure 12a represent the increase rate derived from OMI NO_2 slant column observations over Kiruna. The black boxes in Figures 12c and 12d represent the increase rate measured by FTIR at Zugspitze, data taken from Figure 3b of *Sussmann et al.* [2005]. The grey boxes in Figures 12c and 12d represent the annual mean increase rate at Izaña [*Gil et al.*, 2008]. In the plots, OMI pixels within 100 km of the measurement site were used.

0.5%/K. Therefore, it is likely that the higher summertime stratospheric NO_2 over Antarctica is also related to the Antarctic summer stratosphere being up to 8 K warmer than over the Arctic, owing to radiative (shorter Earth-Sun distance in January) and to dynamical effects [*Rosenlof*, 1996; *Siskind et al.*, 2003].

[52] For midlatitudes, we see a clear annual cycle in stratospheric NO_2, with an amplitude of approximately 1×10^{15} molecules/cm^2. At higher latitudes the seasonal cycle is stronger as a result of the denoxification in winter. In the tropics the amplitude of the seasonal cycle is comparable to the amplitude of semiannual harmonics that, as we will show later, results from the quasi-biennial oscillation (QBO) [*Reed et al.*, 1961]. The weaker seasonal cycle in the tropics reflects the weak seasonal variation in the solar irradiation and the lower stratospheric NO_2 concentration. In the tropics, tropospheric air enters the stratosphere. During the poleward transport by the Brewer-Dobson circulation, N_2O in this imported air is converted into NO_y by the reaction with atomic oxygen. This leads to an increase of stratospheric NO_2 concentration with latitude and a build up of NO_2 in the polar regions.

[53] The QBO is an oscillation in the equatorial zonal winds between 20 and 35 km altitude. The period of the oscillation ranges between 23 and 34 months, with a mean period of 28 months, hence the name quasi-biennial. The QBO in stratospheric ozone has been observed for many years [*Funk and Garnham*, 1962], but its effect was

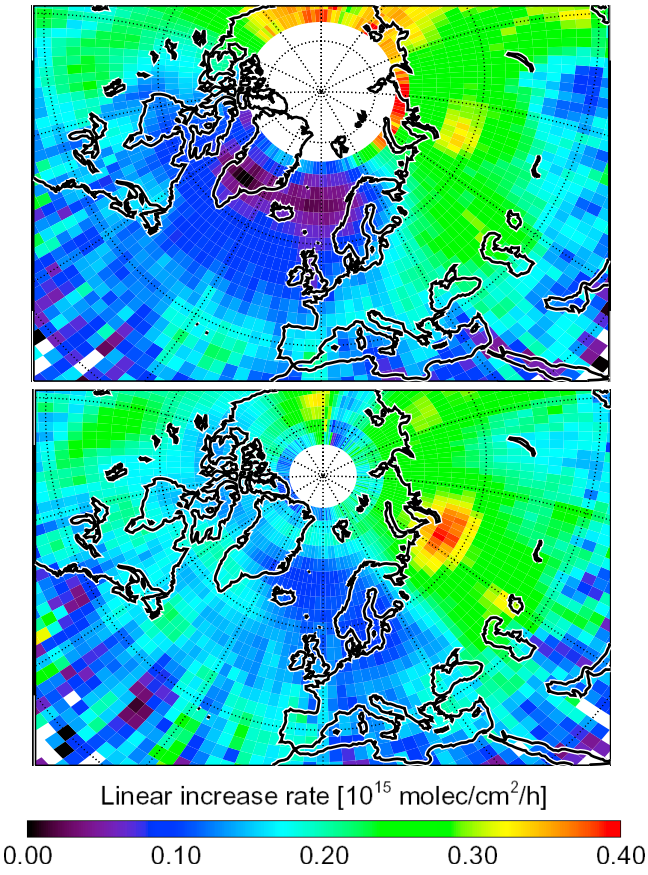

Figure 13. Average diurnal linear increase rate of DOMINO stratospheric NO_2 columns for the Northern Hemisphere for (top) 1–15 March 2005 and (bottom) 16–31 March 2005. The linear increase rate is calculated for locations with two or more OMI overpasses per day.

observed for the first time in stratospheric NO_2 by analysis of altitude-resolved SAGE II measurements [*Zawodny and McCormick*, 1991]. They attribute the NO_2-QBO mainly to QBO-induced modulations in the vertical transport of NO_y in the equatorial region, because changes in the NO_x partitioning due to changes in observed temperature and ozone concentrations are insufficient to explain the NO_2-QBO. Ground-based observations at midlatitudes and high latitudes suggest that the NO_2-QBO is not confined to the tropics: analysis of long-term measurement series reveals a correlation between the QBO cycle and variations in the overhead stratospheric NO_2 column at Lauder [*Liley et al.*, 2000] and over Antarctica [*Cook and Roscoe*, 2009]. *Liley et al.* [2000] propose that the QBO affects stratospheric NO_2 outside the tropics "dynamically," by changing transport rates of relevant chemical species.

[54] We now analyze the OMI NO_2 time series with the multilinear regression methods described by *Zawodny and McCormick* [1991], *Liley et al.* [2000] and *Gruzdev and Elokhov* [2009] in search of the QBO. The employed fitting model

$$y(t) = A_0 + \sum_{i=1}^{3} \Gamma_i + A_4 t + A_5 I_{QBO}(t + \phi_{QBO}) + A_6 I_{SI}(t) + A_7 I_{ENSO}(t + \phi_{ENSO}) \quad (4)$$

(with $\Gamma_i = A_i \sin(\frac{i2\pi t}{365.25}) + B_i \cos(\frac{i2\pi t}{365.25})$ harmonic terms with 12, 6 and 4 month periodicity) contains background (A_0) and linear trend ($A_4 t$). The harmonic terms with 12 and 6 months periodicity describe the annual cycle and the asymmetry between the equinoctial periods, respectively. Additional index terms describe the QBO (I_{QBO}), Solar Index (I_{SI}) and El Niño–Southern Oscillation (I_{ENSO}); ϕ_{QBO} and ϕ_{ENSO} represent the phase (lag) of the QBO and of the ENSO terms, respectively. The QBO index is given by the monthly mean of the zonally averaged equatorial winds at 30 hPa calculated by the NCEP/NCAR Climate Data Assimilation System (http://www.cpc.ncep.noaa.gov/data/indices/qbo.u30.index). The Solar Index I_{SI} is parameterized by the monthly means of the solar radio flux density at 10.7 cm (ftp://ftp.ngdc.noaa.gov/STP/SOLAR_DATA/SOLAR_RADIO/FLUX/Penticton_Absolute/monthly). The ENSO index I_{ENSO} is based on the monthly mean sea level pressure difference between Tahiti and Darwin (http://www.bom.gov.au/climate/current/soihtm1.shtml). I_{QBO}, I_{SI} and I_{ENSO} are scaled to [−1, 1]. Prior to applying the fitting model to the OMI data series, we tested our fitting procedure by reproducing the coefficients reported by *Liley et al.* [2000] for stratospheric NO_2 observed at NDACC station Lauder between 1981 and 1999. As shown in Table 3 we found a trend of +5.2(±0.5)% per decade, which is consistent with the +5% per decade reported by Liley. Similar to their approach we fixed the lag of the QBO and ENSO terms of 140 days and 13 months, respectively. Additional terms were used to account for the El Chichón (April 1982) and Pinatubo (June 1991) eruptions (see *Liley et al.* [2000] for details). The amplitude and lag of the QBO index are free parameters in the fit to the global OMI data set. The SI and ENSO terms were not fitted because these parameters affect the fitting stability at certain latitudes, resulting in an irregular latitudinal dependence of

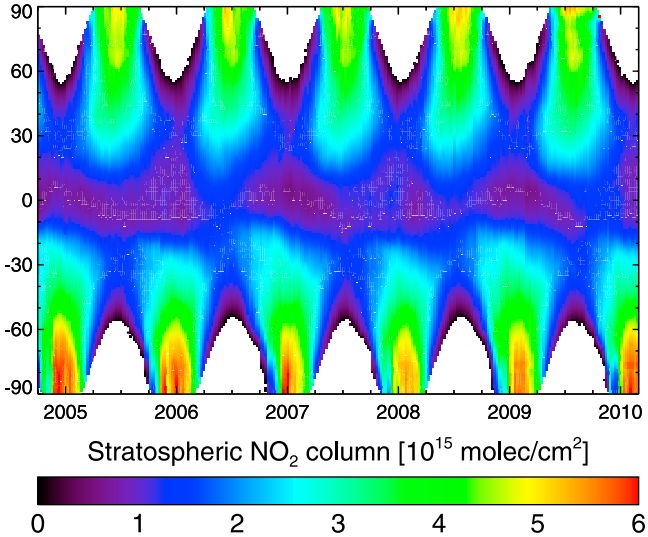

Figure 14. Time series of zonal mean DOMINO stratospheric NO_2 columns as a function of latitude, spanning 1 October 2004 to 1 January 2010. Data are collected in 7 day bins and gridded to 1° × 1°. The plot shows the zonal average in 1°-wide latitude bands. The white regions poleward of 55° denote missing data because of the polar night.

Table 3. Fitted Trends in Ground-Based (Lauder) and Ozone Monitoring Instrument (OMI) Stratospheric NO_2 Over Lauder[a]

	Trend (%/decade)	
Period	Lauder	OMI
1981–1999	5.2(±0.5)	
1981–2010	5.2(±0.5)	
2004–2010	0.4(±2)	
2004–2010		0.6 (±2)

[a]The errors are estimated by varying the length of the fitting window with ±1 year.

the background term, furthermore their contribution to the resulting fit is relatively small.

[55] As a confidence check we also employed the fitting model of *Zawodny and McCormick* [1991], who parameterize the QBO by harmonics with 18, 24 and 30 month periodicity. These harmonic functions adequately parameterize the QBO index for the limited time range of the OMI data set, and this parameterization yields more stable fits than the tabulated monthly mean QBO index. The harmonic fitting model produces the same results as the fitting model based on work by *Liley et al.* [2000]. The fitting model, whose results are presented in Figure 15, shows that the ratio of the NO_2-QBO and the annual term (green trace in Figure 15f) peaks in the tropics with maxima located around 15°S and 5°N. The amplitude of the NO_2-QBO in the tropics is comparable to the annual term, which is illustrated by Figures 15a, 15b and 15e and by Figure 14. The OMI time series show a clear interhemispheric asymmetry in the NO_2-QBO: its peak value is nearly 2 times larger in the Southern Hemisphere than in the Northern Hemisphere. Furthermore the NO_2-QBO peaks at 15°S in the Southern Hemisphere versus 5° in the Northern Hemisphere. This is illustrated by Figures 15a, 15b, 15d and 15e, showing the OMI time series for 5°S, 15°S, 5°N, and 15°N, respectively.

[56] Other studies into the QBO such as those of *Zawodny and McCormick* [1991], *Dunkerton* [2001], *Randel and Wu* [1996], usually report QBO anomalies that are equatorially symmetric in the tropics. However, these studies involve

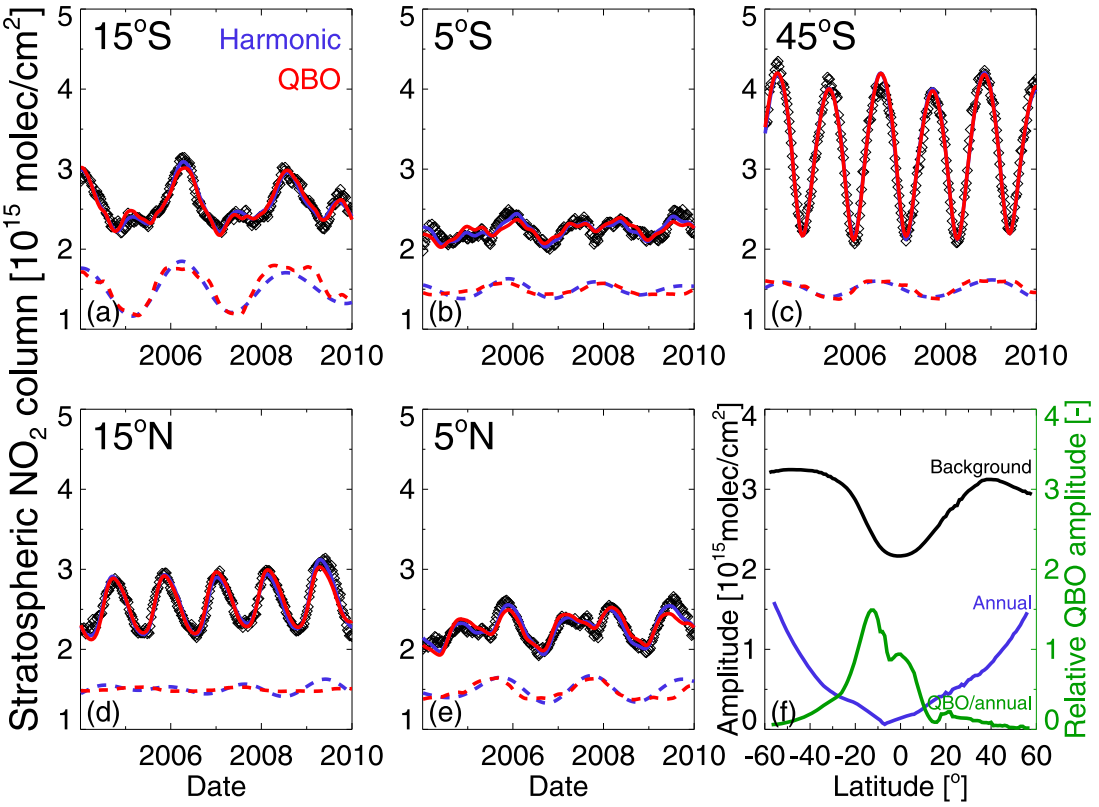

Figure 15. (a–e) Time series of total mean OMI stratospheric NO_2 (black diamonds) and multilinear regression fit (solid line) to the data at selected latitudes. The red trace represents the fit with a model that parameterizes the QBO using the tabulated monthly mean QBO index, and the blue trace represents a fitting model that parameterizes the QBO with harmonic functions of 18, 24, and 30 month periodicity. The dashed lines represent the QBO term in the resulting fit. (f) Background (black), annual (blue), and QBO fitting coefficients for the 2004–2010 OMI stratospheric NO_2 record as a function of latitude. The green trace shows the ratio of the QBO and the annual term (right y axis). The background term corresponds to A_0 in equation (4). The harmonic term Γ_1 in equation (4) yields the annual term via the following trigonometry relations: $a_1 \sin(\frac{2\pi t}{365.25} + \phi) = a_1 \cos(\phi)\sin(\frac{2\pi t}{365.25}) + a_1 \sin(\phi) \cos(\frac{2\pi t}{365.25})$, where $a_1 \cos(\phi)$ and $a_1 \sin(\phi)$ equal the parameters A_1 and B_1, respectively. Then $\phi = \arctan(B_1/A_1)$, and the annual term corresponds to $A_1/\cos(\phi)$.

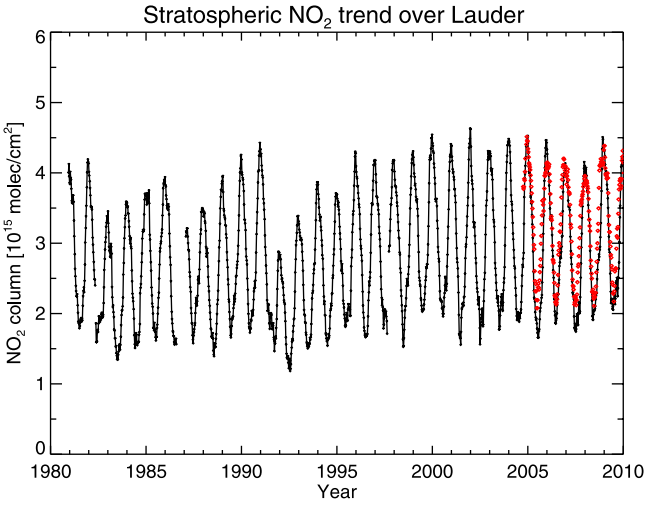

Figure 16. Time series of sunrise stratospheric NO_2 columns measured at Lauder (black line) and collocated DOMINO stratospheric NO_2 columns (red diamonds). Data were averaged in 7 day bins and a three point wide running average filter was applied to remove outliers that occasionally occur in the Lauder series in winter. The Lauder data was downloaded from ftp://ftp.cpc.ncep.noaa.gov/ndacc/station/lauder/ames/uvvis/.

altitude resolved measurements of trace species, whereas OMI observes integrated stratospheric NO_2 columns. Integrated columns based on SAGE II measurements between 25 and 40 km also seem to suggest a stronger NO_2-QBO in the southern tropics [*Zawodny and McCormick*, 1991, Figure 7], the same is seen for integrated GOMOS-observed partial NO_2 columns between 20 and 50 km [*Kyrölä et al.*, 2010, Figure 21].

8.2. Long-Term Trends in Stratospheric NO_2

[57] Figure 16 shows the agreement between collocated OMI stratospheric NO_2 data and the 1981–2010 time series of ground-based stratospheric NO_2 columns measured at Lauder at sunrise. OMI generally reproduces the values of the summer maxima and their year-to-year variability. This shows the potential of instruments such as OMI, and presumably also GOME and SCIAMACHY, to contribute to observing trends in stratospheric NO_2 from space, provided that the data record is of sufficient length.

[58] For the 1981–1999 period *Liley et al.* [2000] report a 5.3% per decade increase in stratospheric NO_2, which is twice the well-known 2.5% per decade increase rate of tropospheric N_2O [*World Meteorological Organization*, 2007]. This increase remains unchanged when the Lauder data record is extended to 2010. (As shown in Table 3, this trend in stratospheric NO_2 over Lauder cannot be reproduced by OMI because of the short time period with measurements.) For the time span of the OMI mission (2004–2010) the Lauder data yields an increase of 0.4(±2)% per decade, which is similar to the 0.6(±2)% per decade increase of stratospheric NO_2 derived from the OMI data over Lauder. For instance, for 1995–2010 we find a trend of +3.0 (±1)% per decade, showing that a 15 year period is also too short to reproduce the trend observed in Lauder between 1981 and 1999 (and 1981–2010).

9. Summary and Conclusions

[59] We have presented stratospheric NO_2 columns obtained from OMI with a data assimilation approach that makes use of the TM4 chemistry transport model. For each OMI observation, we calculate the stratospheric NO_2 column from the TM4 forecast that is based on the analyzed model state. The assimilation of OMI NO_2 total columns in TM4 corrects the tendency of the stratospheric part of the model to diverge from the observations. The scheme is insensitive to tropospheric contributions, and results in a forecast model state that is generally within 0.15×10^{15} molecules/cm^2 of the analysis over remote areas where stratospheric NO_2 dominates the total column.

[60] The evaluation of ground-based techniques for measuring stratospheric NO_2 shows that UV-Vis and FTIR retrievals are only consistent within 15–20% due to inaccuracies in, e.g., the assumed profile and air mass factor, casting some doubt on their usefulness as "ground-truthing" for satellite retrievals. Lacking an alternative, we used ground-based UV-Vis and FTIR measurements from 14 mostly pristine locations in the world to validate the Dutch OMI NO_2 (DOMINO) retrieval (based on data assimilation) and the NASA GSFC Standard Product. OMI retrievals and ground-based estimates of stratospheric NO_2 columns agree on average within 0.3×10^{15} molecules/cm^2 (13%), comparable to the accuracy of the ground-based instruments.

[61] Stratospheric NO_2 retrieved from the DOMINO retrieval on average exceeds the Standard Product by 0.2×10^{15} molecules/cm^2, but on short spatial and time scales, larger biases occur (up to 1×10^{15} molecules/cm^2). Synoptic-scale differences between the two retrievals are explained by differences in the stratospheric air mass factors, and by the spatial smoothing technique used in the Standard Product algorithm. Differences between stratospheric air mass factors can be as high as 8% for specific satellite viewing angles, partly because of interpolation errors in the Standard Product air mass factor look-up table that has only few reference viewing angles. The considerable differences resulting from the air mass factors are dampened by the spatial smoothing (wave-2 fit) in the Standard Product.

[62] The OMI data record runs from October 2004 onward and covers more than 5 years. This allows for the study of temporal variability in stratospheric NO_2 columns on various time scales. During Arctic winter, DOMINO retrievals show low stratospheric NO_2 concentrations within the Arctic polar vortex and higher NO_2 in adjacent regions. The morphology of the stratospheric NO_2 field in the wider vortex area closely resembles the temperature distribution at 50 hPa. A study of day-to-day variability in stratospheric NO_2 shows that DOMINO captures the collapse of the polar vortex during late winter, corroborated by ground-based NO_2 observations over Sodankyla and Jungfraujoch. The early springtime stratospheric NO_2 columns correlate strongly with stratospheric (30–50 hPa) temperatures, reflecting the temperature dependence of the N_2O_5 (photo) dissociation rate and of the NO_x partitioning.

[63] Using the overlapping orbits poleward of 30° latitude, we find that it is possible to observe the diurnal variation in stratospheric NO_2 columns with OMI. At high latitudes (>60°), the diurnal increase rate has a distinct seasonal dependence with a maximum in spring and fall, which is consistent with increase rates inferred from SAOZ measurements at sunrise and sunset. The low increase rates at high latitudes in summer are attributed to the near-depletion of stratospheric N_2O_5, resulting from the long sunlit hours. A map of OMI-derived increase rates shows that in late winter its geographical distribution follows the morphology of the stratospheric NO_2 field with low increase rates inside the denoxified Arctic polar vortex and high increase rates in the NO_x-rich air outside the vortex.

[64] We analyzed the 5+ year time series of DOMINO stratospheric NO_2 columns with a multilinear regression model that includes background, linear trend, and harmonic terms, as well as the quasi-biennial oscillation (QBO). The background and the annual terms are smallest over the tropics and increase gradually toward the poles. Our analysis shows that the QBO in stratospheric NO_2 over the tropics is comparable to the annual term, and stronger over the Southern Hemisphere than over the Northern Hemisphere. The ability to detect long-term trends in stratospheric NO_2, possibly resulting from the well-known positive trend in its N_2O source, with the relatively short OMI satellite data record is limited. Our regression model, when applied to the well-established data record for Lauder, reproduces the previously found +5% per decade in stratospheric NO_2 columns for the 1981–1999 period. This increase remains unchanged when extending the Lauder data record to 2010, but for shorter, more recent periods the derived trend strongly depends on the time range chosen. For the time span of the OMI mission (2004–2010) +0.4% per decade is found, consistent with the trend in collocated OMI stratospheric NO_2 observations over Lauder (+0.6% per decade). The good agreement between the Lauder data record and collocated DOMINO stratospheric NO_2 observations, as well as the first ever space-based observation of diurnal variation in stratospheric NO_2 columns, indicate that OMI makes a valuable contribution to the study of stratospheric NO_2. The issue of long-term trend detection from space deserves further examination; the current OMI data record should be extended with the stratospheric NO_2 columns from the GOME, SCIAMACHY, and GOME-2 measurements.

[65] **Acknowledgments.** We thank Florence Goutail and Andrea Pazmiño for providing the SAOZ data. Karin Kreher is thanked for her assistance with the Lauder data. Michel Van Roozendael and Philipe Demoulin kindly provided (and reanalyzed) the Jungfraujoch FTIR data, and Thomas Blumenstock and Manuel Gil kindly provided Izaña FTIR data. We thank Peter Siegmund and Wim Verkleij for valuable discussions about dynamical processes in the stratosphere. The OMI NO_2 Standard Product was downloaded from http://daac.gsfc.nasa.gov/Aura/data-holdings/OMI/index.shtml. The DOMINO product is freely accessible at http://www.temis.nl/airpollution/no2.html.

References

Anderson, G. P., S. A. Clough, F. X. Kneizys, J. H. Chetwynd, and E. P. Shettle (1986), AFGL Atmospheric Constituents Profiles, *Tech. Rep. AFGL-TR-86-0110*, Air Force Geophys. Lab., Hanscom AFB, Mass.

Beirle, S., S. Kühl, J. Puķīte, and T. Wagner (2010), Retrieval of tropospheric column densities of NO_2 from combined SCIAMACHY nadir/limb measurements, *Atmos. Meas. Tech.*, *3*, 283–299, doi:10.5194/amt-3-283-2010.

Boersma, K. F., E. Bucsela, E. Brinksma, and J. F. Gleason (2002), NO_2, in *OMI Algorithm Theoretical Basis Document*, vol. 4, *OMI Trace Gas Algorithms*, *ATBD-OMI-02 Vers. 2.0*, pp. 13–28, NASA Goddard Space Flight Cent., Greenbelt, Md.

Boersma, K. F., H. J. Eskes, and E. J. Brinksma (2004), Error analysis for tropospheric NO_2 retrieval from space, *J. Geophys. Res.*, *109*, D04311, doi:10.1029/2003JD003962.

Boersma, K. F., et al. (2007), Near-real time retrieval of tropospheric NO_2 from OMI, *Atmos. Chem. Phys.*, *7*, 2103–2118, doi:10.5194/acp-7-2103-2007.

Bovensmann, H., J. P. Burrows, M. Buchwitz, J. Frerick, S. Nöel, V. V. Rozanov, K. V. Chance, and A. P. H. Goede (1999), SCIAMACHY: Mission objectives and measurement modes, *J. Atmos. Sci.*, *56*, 127–150, doi:10.1175/1520-0469(1999)056<0127:SMOAMM>2.0.CO;2.

Bregman, B., A. Segers, M. Krol, E. Meijer, and P. van Velthoven (2003), On the use of mass-conserving wind fields in chemistry-transport models, *Atmos. Chem. Phys.*, *3*, 447–457, doi:10.5194/acp-3-447-2003.

Brohede, S., C. A. Mclinden, G. Berthet, C. S. Haley, D. Murtagh, and C. E. Sioris (2007), A stratospheric NO_2 climatology from Odin/OSIRIS limb-scatter measurements, *Can. J. Phys.*, *85*, 1253–1274, doi:10.1139/P07-141.

Bucsela, E. J., E. A. Celarier, M. O. Wenig, J. F. Gleason, J. P. Veefkind, K. F. Boersma, and E. J. Brinksma (2006), Algorithm for NO_2 vertical column retrieval from the Ozone Monitoring Instrument, *IEEE Trans. Geosci. Remote Sens.*, *44*, 1245–1258, doi:10.1109/TGRS.2005.863715.

Bucsela, E. J., et al. (2008), Comparison of tropospheric NO_2 from in situ aircraft measurements with near-real time and standard product data from OMI, *J. Geophys. Res.*, *113*, D16S31, doi:10.1029/2007JD008838.

Burrows, J. P., et al. (1999), The Global Ozone Monitoring Experiment (GOME): Mission concept and first scientific results, *J. Atmos. Sci.*, *56*, 151–175, doi:10.1175/1520-0469(1999)056<0151:TGOMEG>2.0.CO;2.

Camy-Peyret, C., J.-M. Flaud, J. Laurent, and G. M. Stokes (1983), First infrared measurement of atmospheric NO_2 from the ground, *Geophys. Res. Lett.*, *10*(1), 35–38, doi:10.1029/GL010i001p00035.

Celarier, E. A., et al. (2008), Validation of Ozone Monitoring Instrument nitrogen dioxide columns, *J. Geophys. Res.*, *113*, D15S15, doi:10.1029/2007JD008908.

Chipperfield, M. P., M. L. Santee, L. Froidevaux, G. L. Manney, W. G. Read, J. W. Waters, A. E. Roche, and J. M. Russell (1996), Analysis of UARS data in the southern polar vortex in September 1992 using a chemical transport model, *J. Geophys. Res.*, *101*(D13), 18,861–18,881, doi:10.1029/96JD00936.

Chu, W. P., and M. P. McCormick (1986), SAGE observations of strastospheric nitrogen dioxide, *J. Geophys. Res.*, *91*(D5), 5465–5476, doi:10.1029/JD091iD05p05465.

Clarke, M. R. B. (1980), The reduced major axis of a bivariate sample, *Biometrika*, *67*(2), 441–446, doi:10.1093/biomet/67.2.441.

Cook, P. A., and H. K. Roscoe (2009), Variability and trends in stratospheric NO_2 in Antarctic summer, and implications for stratospheric NO_y, *Atmos. Chem. Phys.*, *9*, 3601–3612, doi:10.5194/acp-9-3601-2009.

Dave, J. V. (1965), Multiple scattering in a non-homogeneous, Rayleigh atmosphere, *J. Atmos. Sci.*, *22*, 273–279, doi:10.1175/1520-0469(1965)022<0273:MSIANH>2.0.CO;2.

de Haan, J. F., P. B. Bosma, and J. W. Hovenier (1987), The adding method for multiple scattering calculations of polarized light, *Astron. Astrophys.*, *183*, 371–391.

De Mazière, M., M. Van Roozendael, C. Hermans, P. C. Simon, P. Demoulin, G. Roland, and R. Zander (1998), Quantitative evaluation of the post-Mount Pinatubo NO_2 reduction and recovery, based on 10 years of Fourier transform infrared and UV-visible spectroscopic measurements at Jungfraujoch, *J. Geophys. Res.*, *103*(D9), 10,849–10,858, doi:10.1029/97JD03362.

Denis, L., H. K. Roscoe, M. P. Chipperfield, M. Van Roozendael, and F. Goutail (2005), A new software suite for NO_2 vertical profile retrieval from ground-based zenith-sky spectrometers, *J. Quant. Spectrosc. Radiat. Transfer*, *92*(3), 321–333, doi:10.1016/j.jqsrt.2004.07.030.

Dentener, F., W. Peters, M. Krol, M. van Weele, P. Bergamaschi, and J. Lelieveld (2003), Interannual variability and trend of CH_4 lifetime as a measure for OH changes in the 1979–1993 time period, *J. Geophys. Res.*, *108*(D15), 4442, doi:10.1029/2002JD002916.

Dobber, M. R., et al. (2006), Ozone Monitoring Instrument calibration, *IEEE Trans. Geosci. Remote Sens.*, *44*, 1209–1238, doi:10.1109/TGRS.2006.869987.

Dobber, M., Q. Kleipool, R. Dirksen, P. Levelt, G. Jaross, S. Taylor, T. Kelly, L. Flynn, G. Leppelmeier, and N. Rozemeijer (2008), Validation of Ozone Monitoring Instrument level 1b data products, *J. Geophys. Res.*, *113*, D15S06, doi:10.1029/2007JD008665.

Douglass, A. R., M. R. Schoeberl, R. B. Rood, and S. Pawson (2003), Evaluation of transport in the lower tropical stratosphere in a global chemistry and transport model, *J. Geophys. Res.*, *108*(D9), 4259, doi:10.1029/2002JD002696.

Dunkerton, T. J. (2001), Quasi-biennial and subbiennial variations of stratospheric trace constituents derived from HALOE observations, *J. Atmos. Sci.*, *58*, 7–25, doi:10.1175/1520-0469(2001)058<0007:QBASVO>2.0.CO;2.

Eskes, H. J., and K. F. Boersma (2003), Averaging kernels for DOAS total-column satellite retrievals, *Atmos. Chem. Phys.*, *3*, 1285–1291, doi:10.5194/acp-3-1285-2003.

Eskes, H. J., P. F. J. van Velthoven, P. Valks, and H. M. Kelder (2003), Assimilation of GOME total ozone satellite observations in a three-dimensional tracer transport model, *Q. J. R. Meteorol. Soc.*, *129*(590), 1663–1681, doi:10.1256/qj.02.14.

Flaud, J.-M., C. Camy-Peyret, D. Cariolle, J. Laurent, and G. M. Stokes (1983), Daytime variation of atmospheric NO_2 from ground based infrared measurements, *Geophys. Res. Lett.*, *10*(11), 1104–1107, doi:10.1029/GL010i011p01104.

Fortuin, J. P. F., and H. M. Kelder (1998), An ozone climatology base on ozonesonde and satellite measurements, *J. Geophys. Res.*, *103*(D24), 31,709–31,734, doi:10.1029/1998JD200008.

Funk, J. P., and G. L. Garnham (1962), Australian ozone observations and a suggested 24-month cycle, *Tellus*, *14*, 378–382, doi:10.1111/j.2153-3490.1962.tb01350.x.

Gil, M., et al. (2008), NO_2 climatology in the northern subtropical region: Diurnal, seasonal and interannual variability, *Atmos. Chem. Phys.*, *8*, 1635–1648, doi:10.5194/acp-8-1635-2008.

Gordley, L. L., et al. (1996), Validation of nitric oxide and nitrogen dioxide measurements made by the Halogen Occultation Experiment for UARS platform, *J. Geophys. Res.*, *101*(D6), 10,241–10,266, doi:10.1029/95JD02143.

Goutail, F., J. P. Pommereau, A. Sarkissian, E. Kyro, and V. Dorokhov (1994), Total nitrogen dioxide at the Arctic polar circle since 1990, *Geophys. Res. Lett.*, *21*(13), 1371–1374, doi:10.1029/93GL01783.

Gruzdev, A. N. (2008), Latitudinal dependence of variations in stratospheric NO_2 content, *Izv. Atmos. Oceanic Phys.*, *44*(3), 319–333, doi:10.1134/S0001433808030079.

Gruzdev, A. N., and A. S. Elokhov (2009), Validating NO_2 measurements in the vertical atmospheric column with the OMI instrument aboard the EOS Aura satellite against ground-based measurements at the Zvenigorod Scientific Station, *Izv. Atmos. Oceanic Phys.*, *45*(4), 444–455, doi:10.1134/S0001433809040057.

Houweling, S., F. Dentener, and J. Lelieveld (1998), The impact of nonmethane hydrocarbon compounds on tropospheric photochemistry, *J. Geophys. Res.*, *103*(D9), 10,673–10,696, doi:10.1029/97JD03582.

Intergovernmental Panel on Climate Change (2007), *Climate Change 2007: The Physical Science Basis. Contribution of Working Group I to the Fourth Assessment Report of the Intergovernmental Panel on Climate Change*, 996 pp., Cambridge Univ. Press, Cambridge, U. K.

Ionov, D. V., Y. M. Timofeyev, V. P. Sinyakov, V. K. Semenov, F. Goutail, J.-P. Pommereau, E. J. Bucsela, E. A. Celarier, and M. Kroon (2008), Ground-based validation of EOS-Aura OMI NO_2 vertical column data in the midlatitude mountain ranges of Tien Shan (Kyrgyzstan) and Alps (France), *J. Geophys. Res.*, *113*, D15S08, doi:10.1029/2007JD008659.

Kerzenmacher, T., et al. (2008), Validation of NO_2 and NO from the Atmospheric Chemistry Experiment (ACE), *Atmos. Chem. Phys.*, *8*, 5801–5841, doi:10.5194/acp-8-5801-2008.

Kyrölä, E., et al. (2010), GOMOS O_3, NO_2, and NO_3 observations in 2002–2008, *Atmos. Chem. Phys.*, *10*, 7723–7738, doi:10.5194/acp-10-7723-2010.

Lamsal, L. N., R. V. Martin, A. van Donkelaar, E. A. Celarier, E. J. Bucsela, K. F. Boersma, R. Dirksen, C. Luo, and Y. Wang (2010), Indirect validation of tropospheric nitrogen dioxide retrieved from the OMI satellite instrument: Insight into the seasonal variation of nitrogen oxides at northern midlatitudes, *J. Geophys. Res.*, *115*, D05302, doi:10.1029/2009JD013351.

Levelt, P. F., G. H. J. van den Oord, M. R. Dobber, A. Mälkki, H. Visser, J. de Vries, P. Stammes, J. O. V. Lundell, and H. Saari (2006a), The Ozone Monitoring Instrument, *IEEE Trans. Geosci. Remote Sens.*, *44*, 1093–1101, doi:10.1109/TGRS.2006.872333.

Levelt, P. F., E. Hilsenrath, G. W. Leppelmeier, G. H. J. van den Oord, P. K. Bhartia, J. Tamminen, J. F. de Haan, and J. P. Veefkind (2006b), Science objectives of the Ozone Monitoring Instrument, *IEEE Trans. Geosci. Remote Sens.*, *44*, 1199–1208, doi:10.1109/TGRS.2006.872336.

Liley, J. B., P. V. Johnston, R. L. McKenzie, A. J. Thomas, and I. S. Boyd (2000), Stratospheric NO_2 variations from a long time series at Lauder, New Zealand, *J. Geophys. Res.*, *105*(D9), 11,633–11,640, doi:10.1029/1999JD901157.

Manney, G. L., N. J. Livesey, C. J. Jimenez, H. C. Pumphrey, M. L. Santee, I. A. MacKenzie, and J. W. Waters (2006), EOS Microwave Limb Sounder observations of "frozen-in" anticyclonic air in Arctic summer, *Geophys. Res. Lett.*, *33*, L06810, doi:10.1029/2005GL025418.

Martin, R. V., et al. (2002a), Interpretation of TOMS observations of tropical tropospheric ozone with a global model and in situ observations, *J. Geophys. Res.*, *107*(D18), 4351, doi:10.1029/2001JD001480.

Martin, R. V., et al. (2002b), An improved retrieval of tropospheric nitrogen dioxide from GOME, *J. Geophys. Res.*, *107*(D20), 4437, doi:10.1029/2001JD001027.

Mount, G. H., D. W. Rusch, J. F. Noxon, J. M. Zawodny, and C. A. Barth (1984), Measurements of stratospheric NO_2 from the Solar Mesosphere Explorer Satellite: 1. An overview of the results, *J. Geophys. Res.*, *89*(D1), 1327–1340, doi:10.1029/JD089iD01p01327.

Mount, G. H., R. Sanders, A. Schmeltekopf, and S. Solomon (1987), Visible spectroscopy at McMurdo Station, Antarctica: 1. Overview and daily variations of NO_2 and O_3, austral spring, 1986, *J. Geophys. Res.*, *92*(D7), 8320–8328, doi:10.1029/JD092iD07p08320.

Munro, R., M. Eisinger, C. Anderson, J. Callies, E. Corpaccioli, R. Lang, A. Lefebvre, Y. Livschitz, and A. P. Albinana (2006), GOME-2 on MetOp, in *Atmospheric Science Conference* [CD-ROM], edited by H. Lacoste and L. Ouwehand, *ESA Spec. Publ. 628*, ESA, Paris.

Naudet, J.-P., R. Thomas, D. Rusch, and R. Clancy (1987), Distribution of stratospheric NO_2 at 10 mbar: SME global morphology and comparison to LIMS observations, *J. Geophys. Res.*, *92*(D8), 9863–9867, doi:10.1029/JD092iD08p09863.

Noxon, J. F. (1979), Stratospheric NO_2 2. Global behavior, *J. Geophys. Res.*, *84*(C8), 5067–5076, doi:10.1029/JC084iC08p05067.

Olivier, J., J. Peters, C. Granier, G. Pétron, J. Müller, and S. Wallens (2003), Present and future surface emissions of atmospheric compounds, *POET Rep. 2*, MNP-RIVM, Bilthoven, Netherlands.

Platt, U., and J. Stutz (2008), *Differential Optical Absorption Spectroscopy, Principles and Applications*, 597 pp., Springer, Heidelberg, Germany, doi:10.1007/978-3-540-75776-4.

Pommereau, J. P., and F. Goutail (1988), O_3 and NO_2 ground-based measurements by visible spectrometry during Arctic winter and spring 1988, *Geophys. Res. Lett.*, *15*(8), 891–894, doi:10.1029/GL015i008p00891.

Randall, C. E., D. W. Rusch, R. M. Bevilacqua, K. W. Hoppel, and J. D. Lumpe (1998), Polar Ozone and Aerosol Measurement (POAM) II stratospheric NO_2 1993–1996, *J. Geophys. Res.*, *103*(D21), 28,361–28,371, doi:10.1029/98JD02092.

Randel, W. J., and F. Wu (1996), Isolation of the ozone QBO in SAGE II data by singular-value decomposition, *J. Atmos. Sci.*, *53*, 2546–2559, doi:10.1175/1520-0469(1996)053<2546:IOTOQI>2.0.CO;2.

Reed, R., W. Campbell, L. Rasmussen, and D. Rogers (1961), Evidence of a downward-propagating, annual wind reversal in the equatorial stratosphere, *J. Geophys. Res.*, *66*(3), 813–818, doi:10.1029/JZ066i003p00813.

Richter, A., F. Wittrock, M. Weber, S. Beirle, S. Kühl, U. Platt, T. Wagner, W. Wilms-Grabe, and J. Burrows (2005), GOME observations of stratospheric trace gas distributions during the splitting vortex event in the Antarctic winter of 2002. Part I: Measurements, *J. Atmos. Sci.*, *62*, 778–785, doi:10.1175/JAS-3325.1.

Rinsland, C. P., D. K. Weisenstein, M. K. W. Ko, C. J. Scott, L. S. Chiou, E. Mahieu, R. Zander, and P. Demoulin (2003), Post-Mount Pinatubo eruption ground-based infrared stratospheric column measurements of HNO_3, NO, and NO_2 and their comparison with model calculations, *J. Geophys. Res.*, *108*(D15), 4437, doi:10.1029/2002JD002965.

Roscoe, H. K., et al. (1999), Slant column measurements of O_3 and NO_2 during the NDSC intercomparison of zenith-sky UV-visible spectrometers in June 1996, *J. Atmos. Chem.*, *32*, 281–314, doi:10.1023/A:1006111216966.

Rosenlof, K. H. (1996), Summer hemisphere differences in temperature and transport in the lower stratosphere, *J. Geophys. Res.*, *101*(D14), 19,129–19,136, doi:10.1029/96JD01542.

Sarkissian, A., H. K. Roscoe, D. Fish, M. Van Roozendael, M. Gil, H. B. Chen, P. Wang, J.-P. Pommereau, and J. Lenoble (1995), Ozone and NO_2 air-mass factors for zenith-sky spectrometers: Intercomparison of calculations with different radiative transfer models, *Geophys. Res. Lett.*, *22*(9), 1113–1116, doi:10.1029/95GL01032.

Sassi, F., and M. Salby (1999), Diurnal variations in the middle atmosphere observed by UARS, *J. Geophys. Res.*, *104*, 3729–3739, doi:10.1029/1998JD100068.

Singleton, C. S., et al. (2007), Quantifying Arctic ozone loss during the 2004–2005 winter using satellite observations and a chemical transport model, *J. Geophys. Res.*, *112*, D07304, doi:10.1029/2006JD007463.

Siskind, D. E., S. D. Eckermann, J. P. McCormack, M. J. Alexander, and J. T. Bacmeister (2003), Hemispheric differences in the temperature of the summertime stratosphere and mesosphere, *J. Geophys. Res.*, *108* (D2), 4051, doi:10.1029/2002JD002095.

Solomon, S., and J. Keys (1992), Seasonal variations in Antarctic NO_x chemistry, *J. Geophys. Res.*, *97*(D8), 7971–7978, doi:10.1029/91JD01707.

Solomon, S., G. Mount, and J. Zawodny (1984), Measurements of stratospheric NO_2 from the Solar Mesosphere Explorer satellite: 2. General morphology of observed NO_2 and derived N_2O_5, *J. Geophys. Res.*, *89*(D5), 7317–7321, doi:10.1029/JD089iD05p07317.

Stammes, P. (2001), Spectral radiance modeling in the UV-visible range, in *IRS 2000: Current Problems in Atmospheric Radiation*, edited by W. Smith and Y. Timofeyev, pp. 385–388, A. Deepak, Hampton, Va.

Stammes, P., J. F. de Haan, and J. W. Hovenier (1989), The polarized internal radiation field of a planetary atmosphere, *Astron. Astrophys.*, *225*, 239–259.

Sussmann, R., W. Stremme, J. P. Burrows, A. Richter, W. Seiler, and M. Rettinger (2005), Stratospheric and tropospheric NO_2 variability on the diurnal and annual scale: A combined retrieval from ENVISAT/SCIAMACHY and solar FTIR at the Permanent Ground-Truthing Facility Zugspitze/Garmisch, *Atmos. Chem. Phys.*, *5*, 2657–2677, doi:10.5194/acp-5-2657-2005.

Vandaele, A. C., C. Hermans, P. C. Simon, M. Carleer, R. Colin, S. Fally, M. F. Mérienne, A. Jenouvrier, and B. Coquart (1998), Measurements of the NO_2 absorption cross-section from 42 000 cm^{-1} to 10 000 cm^{-1} (238–1000 nm) at 220 k and 294 k, *J. Quant. Spectrosc. Radiat. Transfer*, *59*(3–5), 171–184, doi:10.1016/S0022-4073(97)00168-4.

Vandaele, A. C., et al. (2005), An intercomparison campaign of ground-based UV-visible measurements of NO_2, BrO, and OClO slant columns: Methods of analysis and results for NO_2, *J. Geophys. Res.*, *110*, D08305, doi:10.1029/2004JD005423.

van der A, R. J., M. A. F. Allaart, and H. J. Eskes (2010), Multi sensor reanalysis of total ozone, *Atmos. Chem. Phys.*, *10*, 11,277–11,294, doi:10.5194/acp-10-11227-2010.

Van Roozendael, M., C. Fayt, D. Bolsée, P. C. Simon, M. Gil, M. Yela, and J. Cacho (1994), Ground-based stratospheric NO_2 monitoring at Keflavik (Iceland) during EASOE, *Geophys. Res. Lett.*, *21*(13), 1379–1382, doi:10.1029/93GL02433.

Vaughan, G., et al. (1997), An intercomparison of ground-based UV-visible sensors of ozone and NO_2, *J. Geophys. Res.*, *102*(D1), 1411–1422, doi:10.1029/96JD00515.

Vaughan, G., P. T. Quinn, A. C. Green, J. Bean, H. K. Roscoe, M. Van Roozendael, and F. Goutail (2006), SAOZ measurements of NO_2 at Aberystwyth, *J. Environ. Monit.*, *8*, 353–361, doi:10.1039/b511482a.

Wenig, M., N. Spichtinger, A. Stohl, G. Held, S. Beirle, T. Wagner, B. Jähne, and U. Platt (2003), Intercontinental transport of nitrogen oxide pollution plumes, *Atmos. Chem. Phys.*, *3*, 387–393, doi:10.5194/acp-3-387-2003.

Wenig, M., S. Kühl, S. Beirle, E. Bucsela, B. Jähne, U. Platt, J. Gleason, and T. Wagner (2004), Retrieval and analysis of stratospheric NO_2 from the Global Ozone Monitoring Experiment, *J. Geophys. Res.*, *109*, D04315, doi:10.1029/2003JD003652.

World Meteorological Organization (2007), Scientific assessment of ozone depletion: 2006, *Tech. Rep. 50*, Geneva, Switzerland.

Zawodny, J. M., and M. P. McCormick (1991), Stratospheric Aerosol and Gas Experiment II measurements of the quasi-biennial oscillations in ozone and nitrogen dioxide, *J. Geophys. Res.*, *96*(D5), 9371–9377, doi:10.1029/91JD00517.

K. F. Boersma, H. J. Eskes, and P. F. Levelt, Royal Netherlands Meteorological Institute, Wilhelminalaan 10, NL-3732 AE De Bilt, Netherlands. (dirksen@wew.fu-berlin.de)

E. J. Bucsela, SRI International, 333 Ravenswood Ave., 404-57, Menlo Park, CA 94025, USA.

R. J. Dirksen, Institut für Weltraumwissenschaften, Freie Universität Berlin, Carl-Heinrich-Becker-Weg 6-10, D-12165 Berlin, Germany. (dirksen@wew.fu-berlin.de)

D. V. Ionov, Department of Atmospheric Physics, Research Institute of Physics, Ulyanovskaya Str. 1, 198904 St. Petersburg, Russia.

H. M. Kelder, Department of Applied Physics, Eindhoven University of Technology, PO Box 513, NL-5600 MB Eindhoven, Netherlands.